공학박사학위논문

Enhanced understanding of 3D-field-driven toroidal rotation on plasma stability and transport

3D 자기장이 구동하는 토로이달 회전을 통한 플라즈마 안정성 및 수송 연구

2019 년 2 월

서울대학교 대학원

에너지시스템공학부

양 성 무

공학박사학위논문

Enhanced understanding of 3D-field-driven toroidal rotation on plasma stability and transport

3D 자기장이 구동하는 토로이달 회전을 통한 플라즈마 안정성 및 수송 연구

2019 년 2 월

서울대학교 대학원

에너지시스템공학부

양 성 무

Enhanced understanding of 3D-field-driven toroidal rotation on plasma stability and transport

3D 자기장이 구동하는 토로이달 회전을 통한 플라즈마 안정성 및 수송 연구

지도교수 나 용 수

이 논문을 공학박사 학위논문으로 제출함

2019 년 1 월

서울대학교 대학원

에너지시스템공학부 원자핵공학전공

양 성 무

양 성 무의 공학박사 학위논문을 인준함

2018 년 12 월

위 원 장	함택수	(인)
부위원장	나용수	(인)
위 원	황용석	(인)
위 원	인용균	(인)
위 원	고원하	(인)

Abstract

Seong Moo Yang
Department of Energy Systems Engineering
The Graduate School
Seoul National University

A small non-axisymmetric (3D) magnetic field can significantly alter the stability and confinement of tokamak plasmas. Its fundamental mechanics is often associated with electromagnetic torque due to the toroidal symmetry breaking and thus corresponding toroidal rotation, which plays an important role to affect various macro-instabilities as well as transport related to micro-instabilities. This thesis presents various investigations on the torque and rotation evolution under 3D magnetic fields applied to KSTAR tokamak plasmas, and contributions to enhanced understanding for a few major consequences; such as disruptive rotation and plasma collapse due to resonant torque referred to as locked mode (LM), and slowly evolving rotation towards new momentum balance due to non-resonant torque referred to as neoclassical toroidal viscous (NTV) transport.

LMs are observed when the resonant 3D field is strong enough to break the torque balance against viscous torque and then drive a forced reconnection on resonant surfaces. Empirical database across multiple tokamaks indicates that resonant field thresholds for LMs are almost linearly scaled with plasma

density, while a much weaker density dependence appeared in KSTAR. Once a certain confinement regime is separately considered, the linear density dependence is recovered even in KSTAR, though. On the other hand, this suggests that the momentum transport, which is likely to contribute to mode-locking, would be subject to change, depending on the confinement regimes. The momentum transport in tokamak plasmas are known to be dominated by turbulent micro-instabilities. Also, it is well known that non-diffusive properties of the momentum transport can be quantitatively inferred from torque modulation experiments. However, such transient analysis must be taken more carefully than had been traditionally reported methods, in that the modulation technique is inherently accompanied with uncertainty in particle or heat transport channels. Our study explains the possible discrepancy of inferred momentum pinch term when the torque is modulated by neutral beam rather than by non-resonant 3D field, since neutral beam injection can significantly perturb ion temperature as well as beam torque. Another important accomplishment in this thesis lies in the confirmation of global acceleration of plasma rotation by 3D field due to radially drifting electrons. This observation is verified by a kinetically self-consistent magnetohydrodynamic modeling, which offers the quantitative agreement on the co-current plasma spinning in electron-dominated regime observed in the experiments.

Experimental studies in KSTAR helped us understand the 3D field effect. The plasma response can be explained by the ideal MHD, but resistivity should be considered in certain conditions, as well. The future investigation of applicable model and its feasibility needs to be further pursued at various operating conditions

Keywords: Tokamak, Plasma rotation, 3D field, KSTAR, NTV, Mode locking,

Momentum transport

Student Number: 2013-21021

Contents

List of Figures

Chapter 1

Introduction

There are various energy sources that human can utilize in the Earth. Among the various resources, the energy becomes extremely important as human life relies more on the high-tech industries which require a significant amount of energy. Among the various energy sources, nuclear fusion energy has a strong potential to be a future energy. Its fuel exists abundantly in the Earth's ocean and it is relatively harmless than other energy sources.

Nuclear fusion is a fundamental source of energy in the universe. Various stars including Sun generate energy by the nuclear fusion reaction. During the process, more than one nucleus combines and lose mass, and the loss of the mass result to the release of energy according to the energy conservation law. While there are a lot of examples in the universe which show that nuclear fusion reaction can generate energy, fusion reactions are difficult to manipulate for practical purposes. It is challenging to make nuclear fusion reaction in the Earth, as the enormous amount of energy is needed to overcome the repulsion of the nucleus as they get closer. A substantial amount of energy is needed to produce a fusion reaction.

One of the possible ways to generate a fusion reaction is by heating the fuels. When the fuels reaches a certain temperature by heating, nuclear fusion reactions become favorable than other reactions. The favorable temperature level for fusion reaction depends on the type of fuels. D-T reaction is one of the fusion reaction processes which requires relatively small amount of input energy given by,

$$ {}^{2}_{1}D + {}^{3}_{1}T \rightarrow {}^{4}_{2}He\,(3.50MeV) + {}^{1}_{0}He\,(14.1MeV)\,. \tag{1.1} $$

This D-T reaction becomes favorable at very high temperature, where its favorable temperature is around 100,000,000 K. This extremely high temperature with sufficiently high fuel density should be reached, for fusion reaction to be economically feasible. At this high temperature, particles become fully ionized and therefore becomes so-called plasma state; the fourth state of matter.

1.1 Tokamak

For the efficient construction of the fusion reactor, smaller size of the fusion reactor would be favorable. Although a Sun is a successful example of a fusion reactor which uses gravitational force to confine plasmas, fusion reactor with gravitational force is inappropriate for practical use. Instead, we can use magnetic fields to confine the plasmas for practical purposes. A tokamak is one of the magnetic confinement concepts. Unlike other linear magnetic confinement device, particles cannot escape at each end in the tokamak. The tokamak is designed to prevent the particle loss at the ends by bending the linear device into a circle. This toroidal geometry intrinsically have non-uniform structure

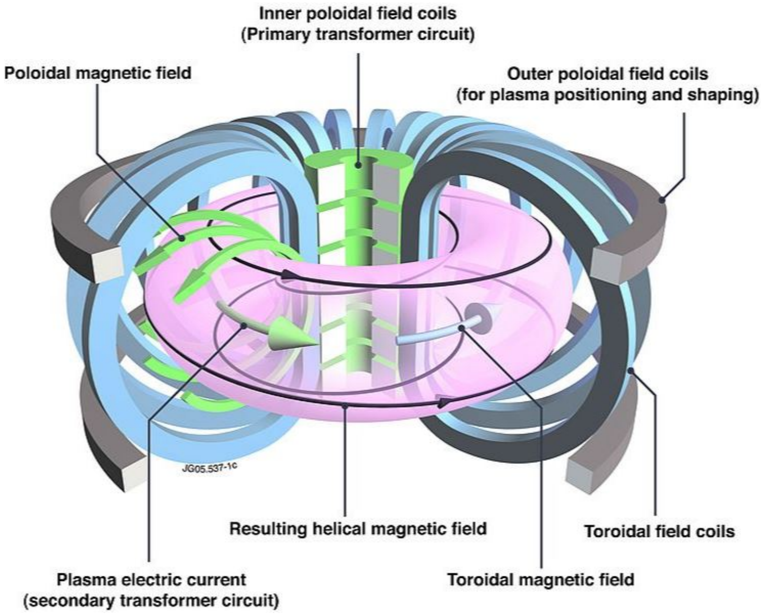

Figure 1.1 Schematic view of the tokamak with plasma current and magnetic field [1].

and makes it physics to be more complicated than other devices. Its structure is shown in Figure 1.1.

The tokamak is one of the promising magnetic confinement concepts and has been investigated for several decades. Experiments in conventional tokamaks show a potential of the tokamak as a power plant by reaching high plasma performance. For investigating its practical use, International Thermonuclear Experimental Reactor (ITER) is being built in France, which is based on the extensive international collaboration.

The performance of the tokamak plasmas strongly relies on their confinement and stability. The confinement is strongly related to the economic efficiency of tokamaks because there could be a less heating power required to heat the plasmas if they can be confined well. The stability is another critical issue, because plasmas can be disrupted if there are any violent instabilities in the plasmas. Its physics should be clarified for understanding the performance of existing tokamaks and future tokamaks including ITER.

1.2 Plasma rotation

Plasmas in tokamak usually have a flow, which is often called as a plasma rotation. The plasma rotation is found to play a vital role in the plasma performance by affecting the MHD instabilities and confinement of the plasmas. It has been found that rotation can stabilize MHD instabilities known as Resistive Wall Mode (RWM) [6], which limits the performance of the plasmas. Various other MHD instabilities, such as Neoclassical Tearing Mode (NTM) are found to be stabilized by the plasma rotation [7].

Plasma rotation also affects the confinement of the plasmas by affecting micro-instabilities in the plasmas. The micro-instabilities, which is known as

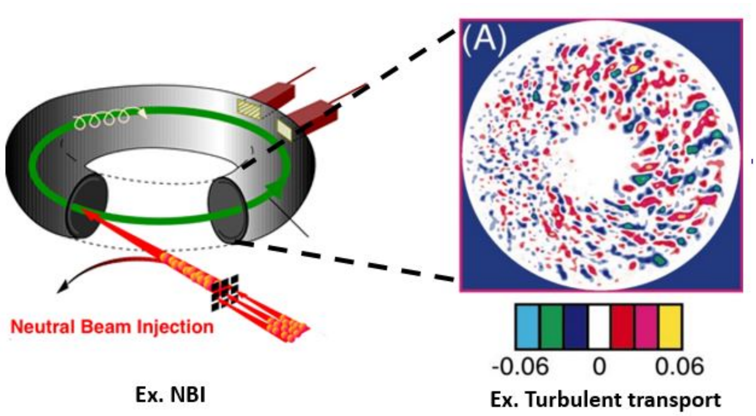

Figure 1.2 Schematic view of (a) Neutral beam injection, turbulent transport [2] and in tokamak plasmas

turbulent transport, are known to determine the confinement properties of the fusion plasmas. Several studies show that $E \times B$ shearing rate can suppress the turbulent transport [8–10], where the radial electric field of tokamaks is determined by radial force balance relation $E = U \times B$. For example, it has been found that enhanced tokamak operation mode can be accessed by suppression of turbulent transport by $E \times B$ shearing.

In usual, plasma rotation refers to the toroidal rotation. A main drive of the toroidal rotation in conventional tokamaks is Neutral Beam Injection (NBI). NBI is usually directed to the toroidal direction in the tokamaks and transfer its momentum to main plasmas. The fast ion transfers a toroidal momentum to the plasmas and drive the toroidal rotation, and the source would be balanced by momentum transport which is known to be governed by micro-instabilities, turbulent transport. Therefore, both momentum sources and its transport should be quantified for predicting toroidal rotation in the axisymmetric tokamaks.

Toroidal rotation can be described by the angular momentum balance equation which can be given by

$$\frac{\partial L_\phi}{\partial t} \simeq -\left\langle e_\phi \cdot \nabla \cdot \overleftrightarrow{\pi}_{i\perp} \right\rangle + \frac{1}{V'}\frac{\partial}{\partial \rho}\left\langle V'\Pi_\phi \right\rangle + \left\langle e_\phi \cdot \Sigma S \right\rangle . \tag{1.2}$$

The first term in the Right Hand Side (RHS) represents classical and neoclassical term, the second term stands for the turbulent Reynolds stress and 3rd term represents momentum sources. This equation shows that toroidal rotation would be determined by the balance between momentum transport and momentum sources.

1.3 Effect of 3D field on toroidal rotation

It is widely known that a presence of small non-axisymmetric field can change the plasma rotation. This is practically interesting, since there can be a various 3D field sources in the tokamak plasmas. The 3D field can exist due to (1) The imperfection of coil fabrication (Error field), (2) The finite number of toroidal coils (TF ripple) (3) External 3D field coils. In particular, the external 3D field is planned to be equipped in future devices such as ITER, due to its great success in ELM suppression experiments [4]. So, understanding the effect of the 3D field on toroidal rotation becomes a practically important issue for utilizing external 3D field coils to have rotation control capability.

Including the effect of the 3D field, toroidal rotation can be expressed as follows [11],

$$\begin{aligned}\frac{\partial L_\phi}{\partial t} \simeq &-\left\langle e_\phi \cdot \nabla \cdot \overleftrightarrow{\pi}_{i\perp} \right\rangle + \frac{1}{V'}\frac{\partial}{\partial \rho}\left\langle V'\Pi_\phi \right\rangle + \left\langle e_\phi \cdot \Sigma S \right\rangle \\ &+ \left\langle e_\phi \cdot \nabla \cdot \overleftrightarrow{\pi}^{3D}_{i\parallel} \right\rangle + \left\langle e_\phi \cdot \overline{\delta J \times \delta B} \right\rangle \end{aligned} \tag{1.3}$$

which includes additional two terms on the RHS in equation (1.2). The fourth term on the RHS represents Neoclassical Toroidal Viscosity (NTV) and the fifth term represent the resonant electromagnetic torque at the mode rational surface.

The NTV represents non-ambipolar radial particles fluxes Γ^{na} by the bounce-averaged radial drift of particles by 3D field [12]. The non-ambipolar flux can be related torque by the 'flux-friction relation' [13]. The NTV is often referred as "nonresonant" torque since it induces torque without causing a substantial change of the plasma parameter unlike magnetic reconnection which is often accompanied by the change of other plasma parameters. Its direct effect only changes the anisotropic pressure tensor and thereby toroidal rotation. Still, change of the toroidal rotation by NTV can change the confinement and stability of the plasmas.

Another type of torque by the 3D field is resonant torque, which can exist at the mode rational surface [14]. The 3D fields with the same helicity with respect to equilibrium magnetic field can resonant to a plasma and exerts torque at the mode rational surface. This effects are often accompanied by the non-ideal MHD effect at the mode rational surface. This resonant torque can lead to an opening the magnetic island, which often leads to the degradation of plasma confinement [14]. Further growth of this island can lead to a termination of discharge, known as plasma disruption.

1.4 Objectives and outline of this dissertation

A presence of the 3D field can change the plasma rotation and thereby affect stability and confinement properties of the plasmas. These effects are investigated in this disseration based on the 3D field experiments in KSTAR by utilizing KSTAR 3D coils shown in Fig. 1.3.

Chapter 2 presents mode locking thresholds in KSTAR. An empirical density

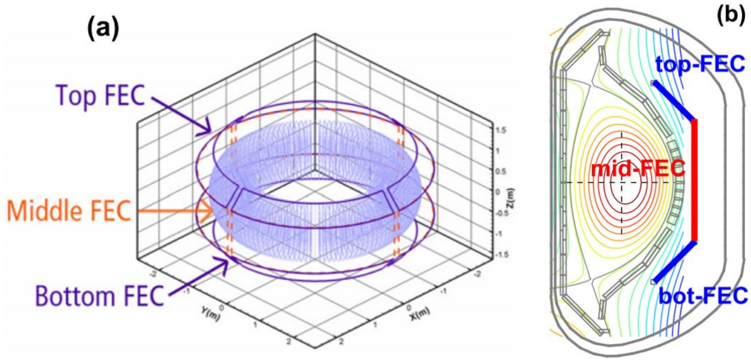

Figure 1.3 (a) KSTAR IVCC coil structure in 3D [3], (b) the reference equilibrium with three poloidal FEC coils [4]

dependence is investigated in KSTAR experiments. Some possible candidates to explain the observed weak density dependence are introduced.

Chapter 3 describes perturbative momentum transport experiments in KSTAR to investigate the momentum pinch term. In particular, a role of ion temperature perturbation in perturbative analysis has been quantified using NRMP and NBI modulation experiments.

Chapter 4 presents acceleration of toroidal rotation by 3D field. It has been found that plasma rotation can be accelerated to the co-current direction by 3D magnetic field. We find that the acceleration observed in KSTAR is originated by resonant $\delta\vec{B}$ amplified due to resistive field penetration, self-consistently regulated by accompanying non-ambipolar electron currents.

Finally, Chapter 5 summarizes all the above chapters and discusses future work.

Chapter 2

Formation of locked mode by rotation deceleration

A presence of the 3D magnetic field can cause a disruptive 3D MHD instability known as the locked mode. Locked mode often leads to the disruption of the plasma, and therefore it is essential to avoid or mitigate the locked mode for safer plasma operation. It is known that plasma locking occurs by the electromagnetic torque at the mode rational surface by the non-ideal effect [14]. At the specific level of electromagnetic torque, plasma rotation which was shielding the formation of magnetic islands becomes not sufficient and this leads to the opening of the magnetic island. This is often called error field penetration, as an intrinsic error field often causes mode locking. In KSTAR, these error field driven mode also occurs by increasing resonant field and also induces the disruption of the plasmas as shown in Fig. 2.1.

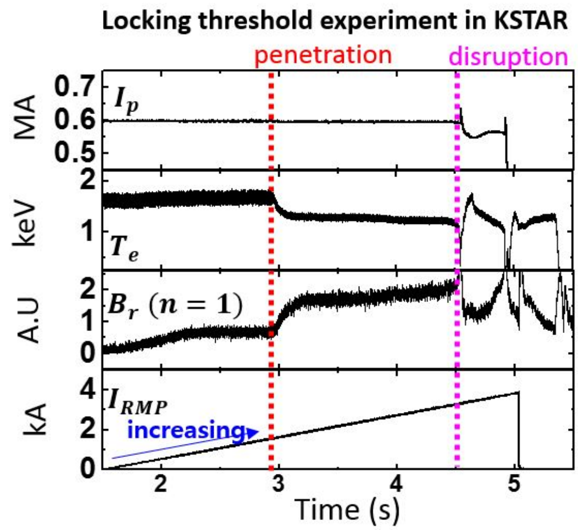

Figure 2.1 Time histories of $n = 1$ locked mode excitation by B_r penetration in KSTAR ohmic discharge. Signatures of mode locking include decrease and modification of the sawtooth behavior, as well as the response seen on the magnetic diagnostics.

2.1 Empirical density scaling

The avoidance of the locked mode formation strongly relies on the empirical scaling of the error field threshold observed in various devices. The error field threshold experiments are done in various devices to investigate its physics and also to avoid the error field driven mode in future devices such as ITER. The error field thresholds are estimated typically by decreasing the density until the fixed external currents in the coils produce a locking, or measuring the critical external currents or the field while holding the plasma density constant. These are allowed since the density dependence of the locking thresholds are very clear in various devices [15]. The threshold scaling studies can be applied for estimating allowable engineering error field for designing toroidal field coil, and also can be used for estimating accessible RMP operation windows. Various parametric dependences have been investigated as a function of toroidal magnetic field B_T, major radius (R), safety factor q_{95} and density are investigated in the previous studies. While parameter dependence of other parameters has strong device dependence, very successful empirical scalings can be obtained with its density dependence. There is almost linear density dependence observed in various devices including DIIID, JET, COMPASS-D [15], Alcator-Cmod [16], MAST [17], and NSTX-U [18]. The multi-machine comparison study as ITPA activities also supports the scaling. However, there also exist other examples in some devices which shows weaker density dependence [19]. Although strong empirical density scaling is common for various studies, some exceptional cases cannot simply be ignored. So, its physics need to be clarified by experimental analysis for its reasonable explanation.

2.2 Theoretical understanding of density scaling

In ideal MHD, all external 3D field components would be shielded by the ideal MHD constraint that $\delta B_{r,m/n}$ component should vanish at mode rational surface due to a delta function shielding current $\delta J_{\|,m/n}$ which exerts no toroidal torque on the plasmas. So, the inclusion of the non-ideal MHD effect, which allows shielding current $\delta J_{\|,m/n}$ to cause a nonzero $\delta B_{r,m/n}$ component on the rational surface is required to explain the locked mode formation. This non-ideal MHD effects can produce a local electromagnetic torque called Maxwell-stress torque, which is the source of the locked mode formation. This non-ideal MHD effect becomes significant on the mode rational surface, and the basis of the locked mode theory is determined from the inner-layer dynamic with including various non-ideal MHD effects. The radially localized Maxwell-stress torque density can be written by the following form,

$$\begin{aligned}\left\langle \delta J_{\|,m/n} \times \delta B_{m/n} \right\rangle \simeq & - m_i n_i \left(4nc_A^2\right) \left(\frac{\delta B^{vac}_{\rho,m/n}}{B_0}\right)^2 \\ & \times \left[\frac{\omega\tau_s}{\left(-\delta'\right)^2 + \left(-\omega\tau_s\right)^2}\right] \frac{V\delta\left(\rho - \rho_{m/n}\right)}{V'} \end{aligned} \tag{2.1}$$

The localized electromagnetic torque which is shown in Eq. (2.1) tries to relax the rotational at the mode rational surface. This localized torque can induce the strong damping of rotation at the mode rational surface, which is compensated by the perpendicular momentum transport. The penetration of mode occurs, once the electromagnetic torque becomes sufficiently strong and plasma can no longer shield the resonant torque. There would be a significant change in the plasma rotation as the magnetic island becomes sufficiently large and affects the plasma rotation.

The theoretical understandings are extensively developed to demonstrate the empirical density dependence. However, the empirical linear density dependence is difficult to explain by the theory, which contains the electromagnetic torque and momentum transport related terms. It has been found that the inclusion of ion NTV term can play a critical role in the linear density scaling and included in the theoretical formulation [20]. After including the ion NTV term, theoretical scaling can also have a capability to explain the density scaling [21], though this depends on the applicable theoretical regime. Based on the previous empirical scaling studies and theoretical works, a widespread understanding of error field threshold is that the density dependence would be generally applicable to most devices.

2.3 Density dependence in KSTAR

KSTAR is a very good place to test the error field threshold study due to its extremely low level of intrinsic error field than other devices [22]. Unlike other devices, there is no need to correct the intrinsic error field in KSTAR, which allows reduced uncertainties in the error field threshold experiments. To investigate the density dependence in KSTAR, error field threshold experiments in KSTAR are done by slowly increasing $n = 1$ field. Once the plasmas reach the error field thresholds, there is an increase of B_r which also accompanied by the reduction of sawtooth activities in the as shown in Fig. 2.1. This can induce the reduction of confinement and eventually lead to the termination of discharges known as plasma disruption.

It is generally accepted that mode locking is the event $q = 2$ surface $q = 2$ surface. This can show what δB_{mn} would be important to estimate the locked mode threshold. To verify what poloidal component can dominantly affect the mode locking in KSTAR, time evolution of toroidal rotation during the mode-

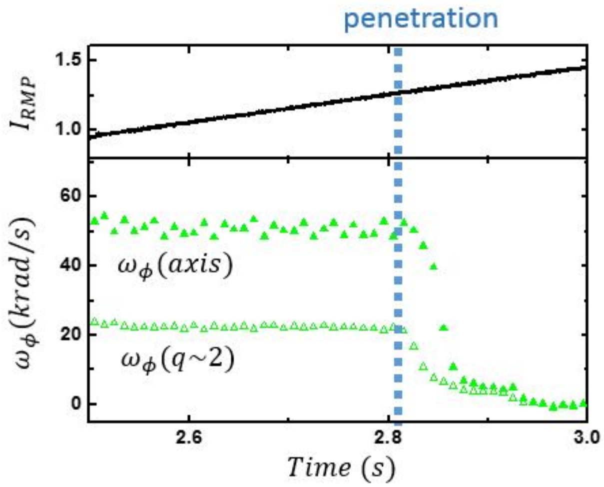

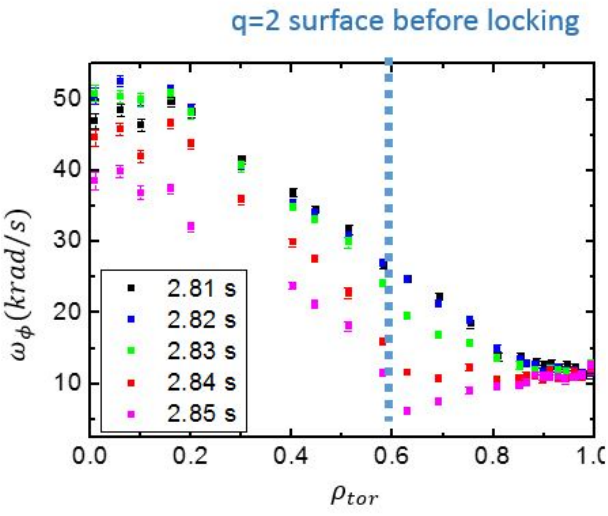

Figure 2.2 (a)Time evolution of I_{IVCC} and plasma rotation at magnetic axis and $q = 2$ surface and (b) plasma rotation profile evolution during the mode locking

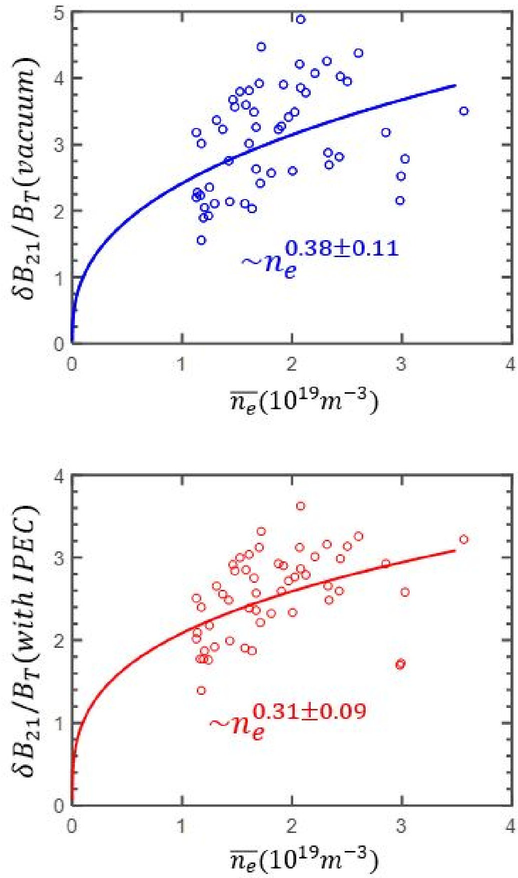

Figure 2.3 Perturbation threshold as a function of line-averaged density $\bar{n}_e$ in KSTAR with (a) vacuum plasma model and (b) ideal MHD plasma response model

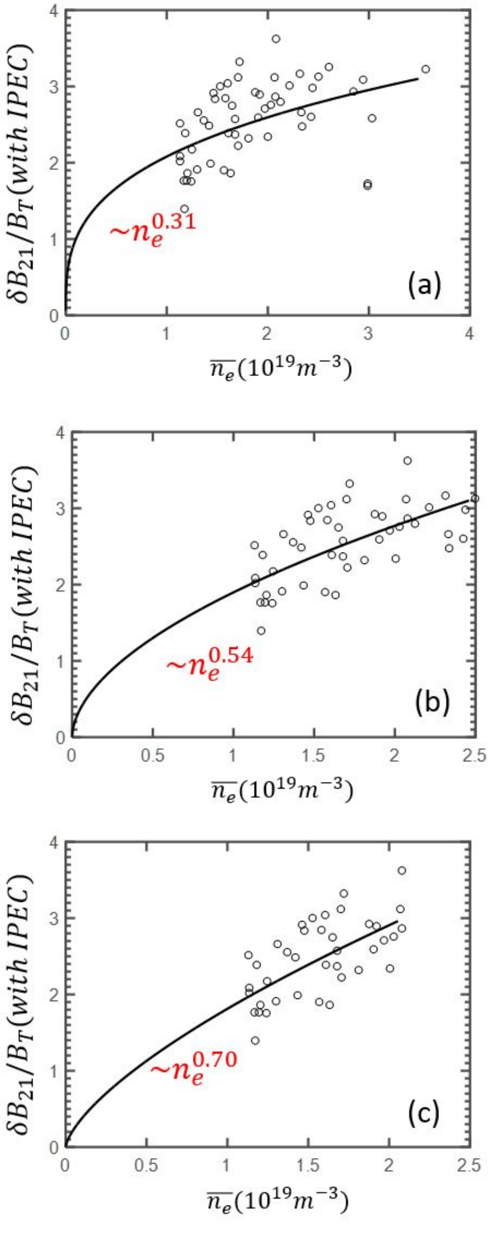

Figure 2.4 Perturbation threshold as a function of line-averaged density $\bar{n}_e$ in KSTAR with (a) including all discharges, (b) excluding the discharges density with $\bar{n}_e > 2.5 \times 10^{19}m^{-3}$, and (c) excluding the discharges density with $\bar{n}_e > 2 \times 10^{19}m^{-3}$

locking is investigated. Fig. 2.2 shows a local decrease of the plasma rotation around $q = 2$ surface. This shows that the locking process in KSTAR is likely to start and occur at the $q = 2$ surface as investigated in the various other devices. Based on this observation, we considered that δB_{21} should be used for error field penetration, which gives the boundary condition of the inner layer problems.

To investigate the density dependence in KSTAR, database with $B_T = 2T$, $I_p = 600kA$ are collected at various plasma densities in ohmic discharges. While inner-layer dynamics would be determined by scaling analysis, its boundary condition can be given by outer layer solution δB, which is estimated by IPEC simulation [23]. Assuming that magnetic islands are small enough, outer layer solution using ideal MHD equation can be useful for estimating the plasma response which includes various important effect such as poloidal mode coupling, shielding current, or kink response. While ideal MHD solution can give insight for the plasma response, we also calculated the perturbed field B_{21} with vacuum plasma response for the comparison. The results are shown in Fig. 2.3. An important implication from Fig. 2.3 is that the density dependence shows no big differences even with the change of the plasma response model. Its density dependence is approximately $\bar{n}_e \approx 0.3$ for both calculations, which is relatively weaker than the result from other devices and multi-machine comparison studies.

In Fig. 2.3, there seems to be a large scattering for relatively higher density discharges for the density scaling. By excluding the discharges in the higher density, one can find that the scaling becomes clearer as shown in Fig. 2.4. That regime dependence of density scaling has been reported in other devices, but no clear explanation has been addressed in previous studies.

2.3.1 Saturation of momentum confinement

In ohmic discharges, it is widely known that there could be a change of confinement regime which depends on the density. This is known as Linear Ohmic Confinement (LOC) to Saturated Ohmic Confinement (SOC) transition. One possible explanation for this behavior is ITG-TEM transition, though it still requires some validation. In KSTAR, energy confinement time can be defined in the stationary conditions as

$$\tau_E = \frac{W_{tot}}{P_{Oh}}. \tag{2.2}$$

where W_{tot} is the total stored energy of plasma and P_{Oh} is ohmic heating power by a central solenoid coil. By calculating the τ_E in KSTAR ohmic discharge, this LOC to SOC transition can be found as shown in Fig. 2.5, which is already reported in the previous study [24]. Interestingly, this regime dependence can be applied to error-field threshold scaling which is investigated in the previous section. In LOC regime, relatively clearer density dependence $\bar{n}_e^{0.7}$ can be found while the dependence can no longer exist and even negative dependence $\bar{n}_e^{-0.3}$ is found once the density reaches the saturated ohmic confinement regime.

This saturation of the confinement time strongly affects to the theoretical scaling analysis. This is because previous studies assumed linear ohmic confinement when deriving the density dependence in ohmic discharges [21], which gives

$$\delta B_r/B_T = \bar{n}_e^1 B_T^{-9/5} R_0^{-1/4} \tag{2.3}$$

in the polarization regime. Apparently, this assumption is not applicable to SOC regime and should be adequately modified to get the proper scaling. Based on the confinement scaling in the L-mode discharges [25] one can get a modified

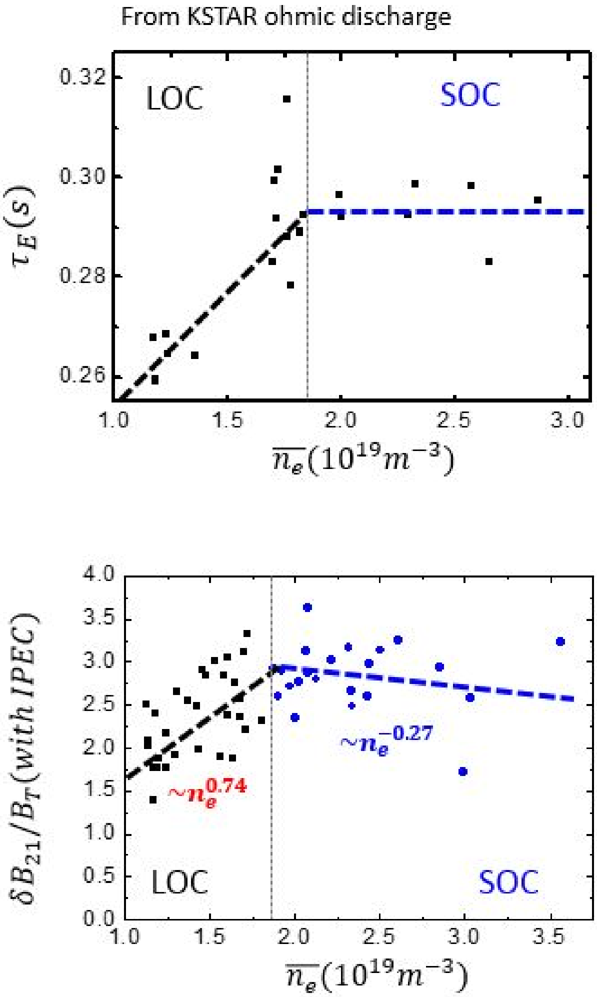

Figure 2.5 Confinement time investigated at the various density ranges and the Perturbation threshold as a function of line-averaged density $\bar{n}_e$ in KSTAR ohmic discharges

scaling in the SOC regime which can be written as

$$\delta B_r/B_T = \bar{n}_e^{4/70} B_T^{-87/70} R_0^{11/70}. \tag{2.4}$$

By comparing the Eqs. (2.3) and 2.4, one can clearly see that there are significant differences in their density dependence. This is consistent to the strong reduction of density dependence shown 2.5 in the KSTAR experiments.

2.3.2 A role of electron NTV

Another critical factor that could affect the density dependence can be a role of the electron NTV. Although electron NTV in $1/\nu$ regime can be ignored due to the high collisionality of electrons than ions, it may not be negligible in the real experiment. For example, if electron temperature is sufficiently larger than ions, electron NTV can play a role in the non-ambipolar process. So, an experimentally relevant plasma parameter should be chosen for estimating the NTV effect. In the KSTAR experiment, we found that electron NTV can accelerate the plasma rotation as demonstrated in the previous section. The acceleration seems to affect the error field threshold as shown in Fig 2.6. This implies that electron NTV can also affect the error field threshold by the acceleration of the plasma rotation.

On the other hand, previous studies only included ion NTV for explaining their density dependence in the error field threshold [20,21]. This means it would be necessary to include the electron NTV term in the error field threshold for its application to KSTAR plasmas. Because the inclusion of electron NTV can cancel out the effect of ion NTV, as there offset frequency would have opposite direction, this can lead further induce the reduction of density dependence in KSTAR.

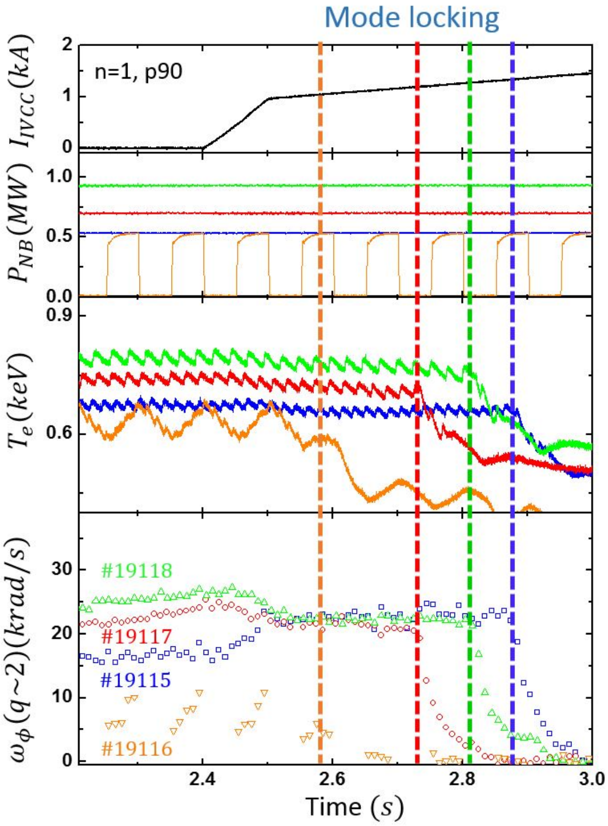

Figure 2.6 The time traces of main plasma parameters in KSTAR discharges. (a) Amplitude of IVCC coil currents, (b) NBI heating power, (c) electron temperature at the $\rho \sim 0.4$, (d) toroidal rotation frequency measured at the $\rho \sim 0.7$ location.

Chapter 3

Momentum transport study using 3D field

The momentum transport plays a very important role in determining the plasma rotation. Unlike heat transport, momentum transport is known to have a strong non-diffusive transport property [26]. The toroidal momentum flux driven by electrostatic turbulence is related to the Reynolds stress term in the angular momentum balance equation [26]. The Reynolds stress may be decomposed as a general form of the momentum transport flux in terms of toroidal velocity v_ϕ:

$$\Pi_\phi \equiv -nmR\chi_\phi \frac{\partial v_\phi}{\partial r} + nmRV_{pinch}v_\phi + \Pi_{res} \tag{3.1}$$

Other than the momentum diffusivity χ_ϕ, non-diffusive terms exist, such as the momentum pinch term V_{pinch} [27, 28], and the residual stress term Π_{res} [26]. Experimentally, this non-diffusive component can be separated by using transient analysis which is often called perturbative analysis. We utilized the distinct properties of 3D magnetic field compare to other actuators (NBI), which allows damping of plasma rotation without change of other parameters.

3.1 Perturbative momentum transport studies

Perturbative analysis has been applied and has successfully shown the non-diffusive properties in the momentum transport from various tokamaks, such as JT-60U [29,30], JFT-2M [31], Alcator C-Mod [32], JET [33,34], DIII-D [35], NSTX [36], KSTAR [24, 37] and MAST [38]. Since the development of scaling and modelling of the momentum transport in future devices is an important issue, multi-machine comparison studies have been carried out to access a wider range of dimensionless parameters [39]. The study suggests robust predictive modelling of momentum transport requires detailed quantitative comparison between simulations and experiments.

The non-diffusive terms found that theory and simulations have been experimentally studied using perturbative analysis with various different methods. In Alcator C-Mod, the momentum pinch term was investigated using rotation change during the L–H transition [32]. In JT-60U and JET, modulated neutral beam injection (NBI) was used [30, 33, 34]. In NSTX, DIIID, KSTAR, and MAST, non- resonant magnetic perturbation (NRMP) or NBI blip was used for the perturbative analysis [24, 35–38]. The results from various tokamaks have been evaluated in multi-machine comparison study, and it was sug- gested that the momentum transport properties in each device could have its own characteristic [39].

One example is the Prandtl number $P_r = \chi_\phi/\chi_i$, the ratio of momentum to ion thermal diffusivity. $P_r > 1$ is observed in JT-60U and JET, while $P_r < 1$ is obtained in NSTX, DIII-D, and Alcator C-Mod. One possibility addressed to explain this feature is the parameter dependence of momentum transport properties. Different operating regimes in each tokamak could result in differences in dimensional and dimensionless parameters, so that the momentum transport properties can differ for each device [39]. Another possibility can be driven by the properties of the actuator in the perturbative experiments. In previous studies, different actuators were applied to each device, and the potential effect of the actuator to momentum transport could differ. For example, neoclassical toroidal viscosity (NTV) from NRMP would have a smaller perturbation to the kinetic profiles of plasmas other than the rota- tion profile. On the other hand, NBI can induce perturbations both to the ion temperature and the rotation profile due to its collisional process, though compensated NBI power or high frequency modulation utilizing j $\times$ B torque could reduce or eliminate the ion temperature perturbation. If the extra perturbation driven by NBI can drive the additional change in trans- port properties by their thermodynamic dependences, this can affect the time constant assumption of transport coefficients used in the previous studies. The consequences of non-constant transport coefficients have been discussed in previous study, though its effect to momentum transport has not been covered [40].

3.2 Design of perturbative experiments in KSTAR

Dedicated experiments are conducted for momentum transport study in KSTAR H-mode plasmas. The major parameters in the discharges are $B_T = 2.6T$ and $I_P = 500kA$. The plasma elongation factor κ is about 1.8, and $q_{95} \approx 8$. This choice of parameters allows a favorable q-profile that has no sawtooth that could possibly affect the momentum transport analysis. The ion temperature and toroidal rotation $\omega_\phi = v_\phi/R$ are measured by charge exchange recombination spectroscopy (CES) [41]. The CES system can provide complete profiles from the plasma edge to the magnetic axis. The line-averaged density measurements are based on microwave interferometry calibrated with far-infrared (FIR) measurement.

As a perturbation source of the toroidal rotation, two actuators, tangential NBI and NRMP are used. Experiments using each actuator is described as follows.

3.2.1 NBI modulation experiment

NBI is used to induce the toroidal rotation perturbation. The effect of NBI on the plasma rotation is clear, and its torque is widely benchmarked with good accuracy compared with other torque sources, though its deposition profile is very broad [42]. Reference Mantica2010 studied and demonstrated the applicability of tangential NBI in time-dependent transport simulations. The torque is mainly injected by the collisional process, and this induces perturbation to the ion temperature, in addition to the toroidal rotation. The experiment uses 50 keV and 0.63 MW NBI with a modulation frequency $f_{mod} = 4$ Hz and a duty cycle $dc = 50$ %, as shown in Fig. 3.1. This is sufficiently slower than the time resolution 10 ms of CES for the rotation measurement. Considering the modulated 4 Hz NBI power with the duty cycle $dc = 50$ %, the total time-averaged NBI power during the analysis becomes 3.14 MW. This allows a similar level of heating power and ion temperature for the comparison study with the NRMP case.

3.2.2 NRMP modulation experiment

NRMP is known to induce additional friction forces and toroidal momentum transport, called NTV torque [12, 43, 44]. NRMP is applied using the In-Vessel

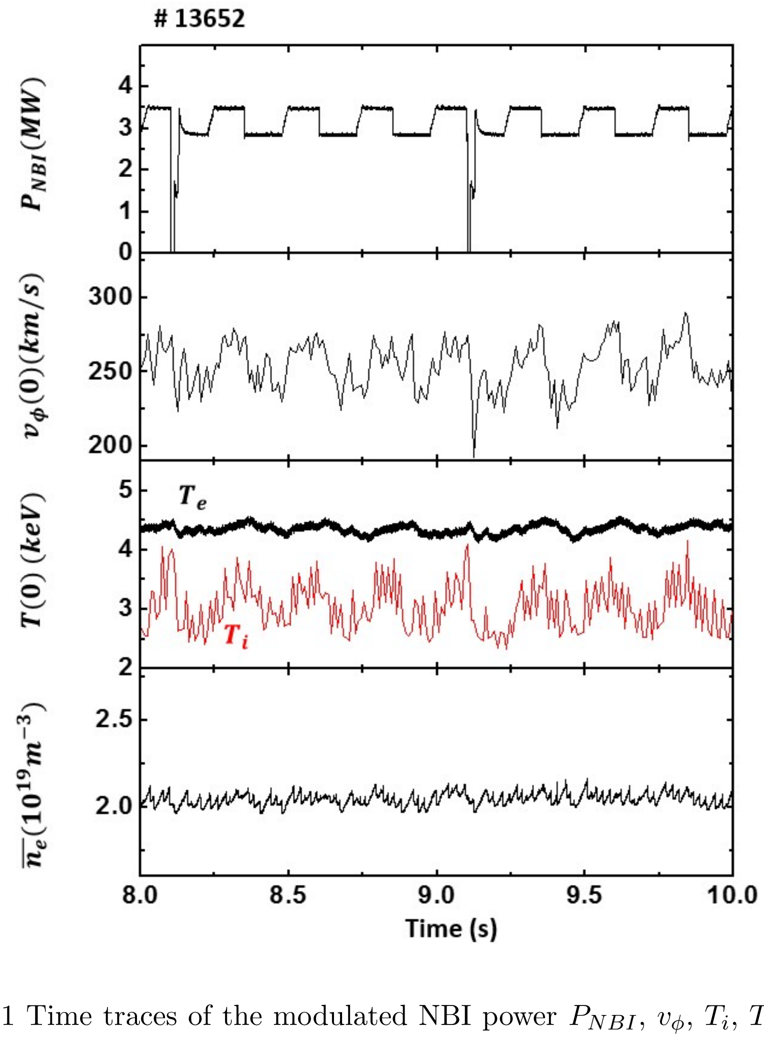

Figure 3.1 Time traces of the modulated NBI power P_{NBI}, v_ϕ, T_i, T_e, and $\bar{n}_e$ for the KSTAR NBI modulation experiment (#13652).

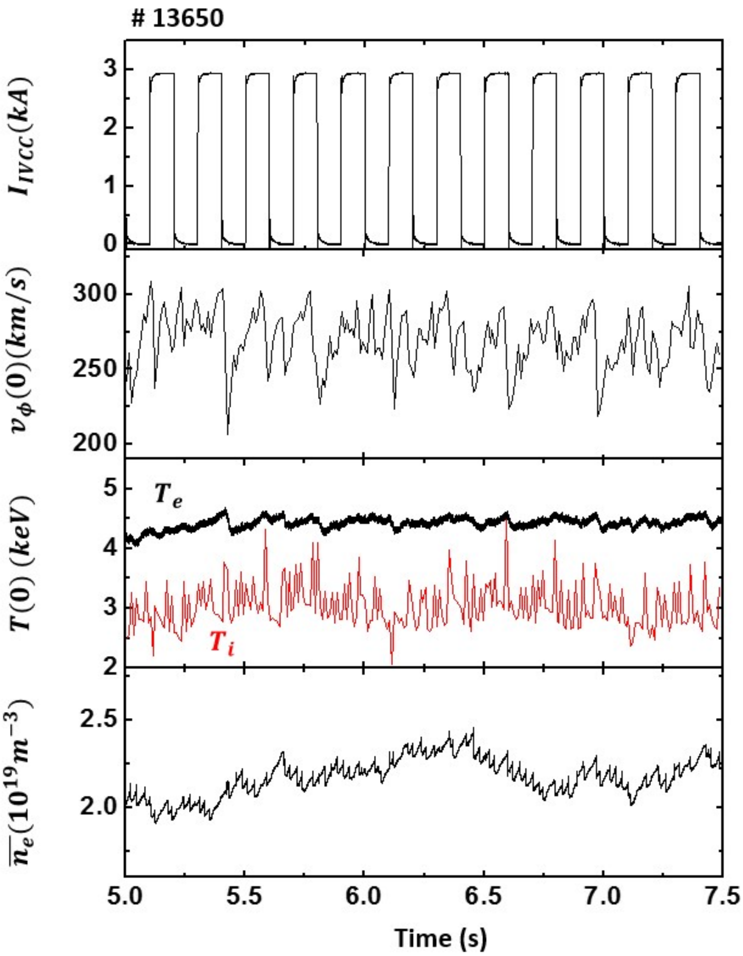

Figure 3.2 Time traces of the modulated I_{IVCC}, v_ϕ, T_i, T_e, and $\bar{n}_e$ for the KSTAR NRMP modulation experiment (#13650).

Control Coil (IVCC) in KSTAR. KSTAR has three rows of IVCC, which allows for highly non-resonant configuration of the NTV torque. The non-resonant effect and strong NTV torque are observed from the experiment using $n = 1$ with the phase = –90° configuration in KSTAR [45]. Furthermore, the simulation, which is described in Section 4, estimates a strongly localized NTV profile in this discharge. The highly localized NTV structure reduces the complicating factor in the perturbative analysis. In the dedicated experiment, this $n = 1$ with phase of –90° NRMP is used as a perturbation source of the rotation. The applied IVCC current is 3 kA, and Fig. 3.2 shows that the modulation frequencies are 5 Hz with the duty cycle of 50 %. This is also sufficiently slower than the time resolution of CES of 10 ms. The total injected NBI power is 3.09 MW.

3.3 Extraction of transport coefficients

3.3.1 The experiments in the modulated NBI case

Figure 3.1 shows the time traces of NBI power (P_{NBI}), core toroidal rotation v_ϕ, core ion temperature T_i (0), core electron temperature T_e (0), and line-averaged density $\bar{n_e}$ for modulation cycles. NBI modulations are applied from (8 to 10) s, and all of the beams are turned off at (8.1 and 9.1) s for 10 ms, to obtain the background CES measurement. Figures 3.1 (b) and (c) show that there is a clear modulation at $f_{mod} = 4$ Hz in v_ϕ and $T_i(0)$, respectively. Figure 3.1 (d) shows that the modulation in the line-averaged density looks unclear, and stays around $\bar{n}_e = 2 \times 10^{19} m^{-3}$. To investigate the effect of the NBI modulation more clearly, the conditional averaging is applied during the modulation cycles. This conditional averaging is to integrate each cycle based on the modulated frequency $f_{mod} = 4$ Hz, by assuming that the plasma is identical during the analysis period. In the conditional average, 6 modulation cycles with $f_{mod} = 4$

Hz are integrated during the modulation from (8.25 to 10) s. Figure 3.3 shows the result of the conditional averaging. In order to see the periodicity of the modulation of NBI, two identical modulations are plotted in Fig. 3.3 from (0 to 0.25) s and from (0.25 to 0.5) s. These clearly show that about 10 % of v_ϕ and T_i are modulated, while T_e and $\bar{n}_e$ is kept constant within 5 %.

The phase and amplitude of the v_ϕ modulation are obtained by Fast Fourier Transform (FFT) analysis. The analysis is carried out at 4 Hz, which is the frequency of the NBI modulation. FFT is applied for the time period from (8.25 to 10) s where the conditional averaging was performed. Figure 3.4 shows radial profiles of the phase and amplitudes of the v_ϕ modulation. Here, the phase values are calculated with respect to the phase of the tangential beam power. It is noteworthy that the radial profiles of the phase are complicated, since the torque is also changing with the power during the NB modulation. Figure 3.5 shows the results of the FFT analysis that is also applied to T_i. A displacement of the whole plasma and Shafranov shift can occur by modulated T_i due to NBI. During the NBI power modulation, this could result in a periodic equilibrium change of the order of ± 10 mm. This can affect the experimental CES measurement at fixed positions in the laboratory frame. Here, time-dependent EFIT reconstructed equilibrium is used to map all the experimental data onto the same flux grid to eliminate this effect [42].

3.3.2 The experiments in the The modulated NRMP case

Figure 3.2 shows the time traces of the IVCC current I_{IVCC}, $v_\phi(0)$, $T_i(0)$, $T_e(0)$, and $\bar{n}_e$ for modulation cycles. While the IVCC current is clearly modulated, its effect on v_ϕ (0), T_i (0), and $\bar{n}_e$ does not look clear. Although all of the beams are turned off at (5.1, 6.1, and 7.1) s for 10 ms to obtain background CES measure-

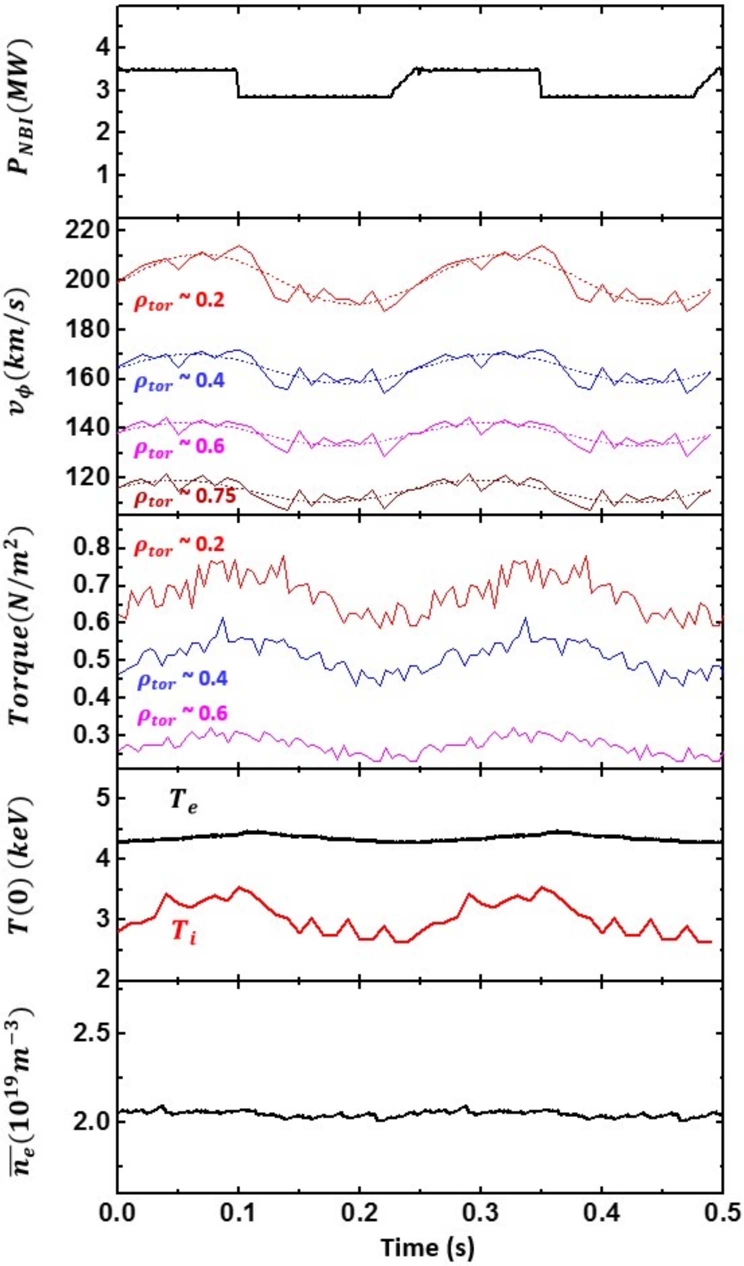

Figure 3.3 Time traces of the conditional averaged P_{NBI}, v_ϕ, Torque density, T, T_e, and $\bar{n}_e$ for the KSTAR NBI modulation experiment (#13652).

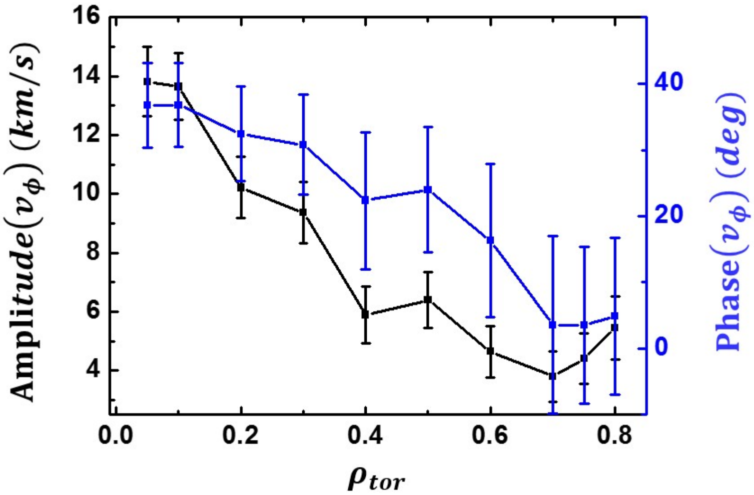

Figure 3.4 Radial profiles of the experimental amplitude and phase of the v_ϕ modulation at 4 Hz for the KSTAR NBI modulation experiment (#13652).

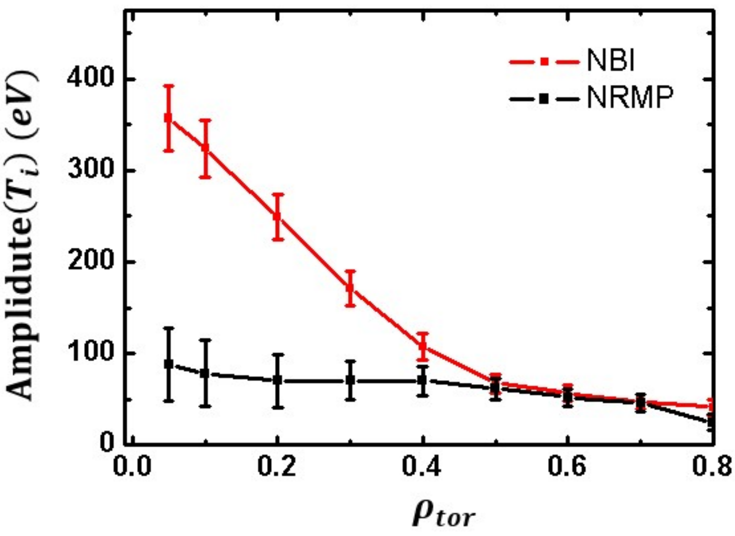

Figure 3.5 Radial profiles of the experimental amplitude of the T_i modulation at 4 Hz for the NBI modulation experiment (#13652), and at 5 Hz for the NRMP modulation experiment (#13650).

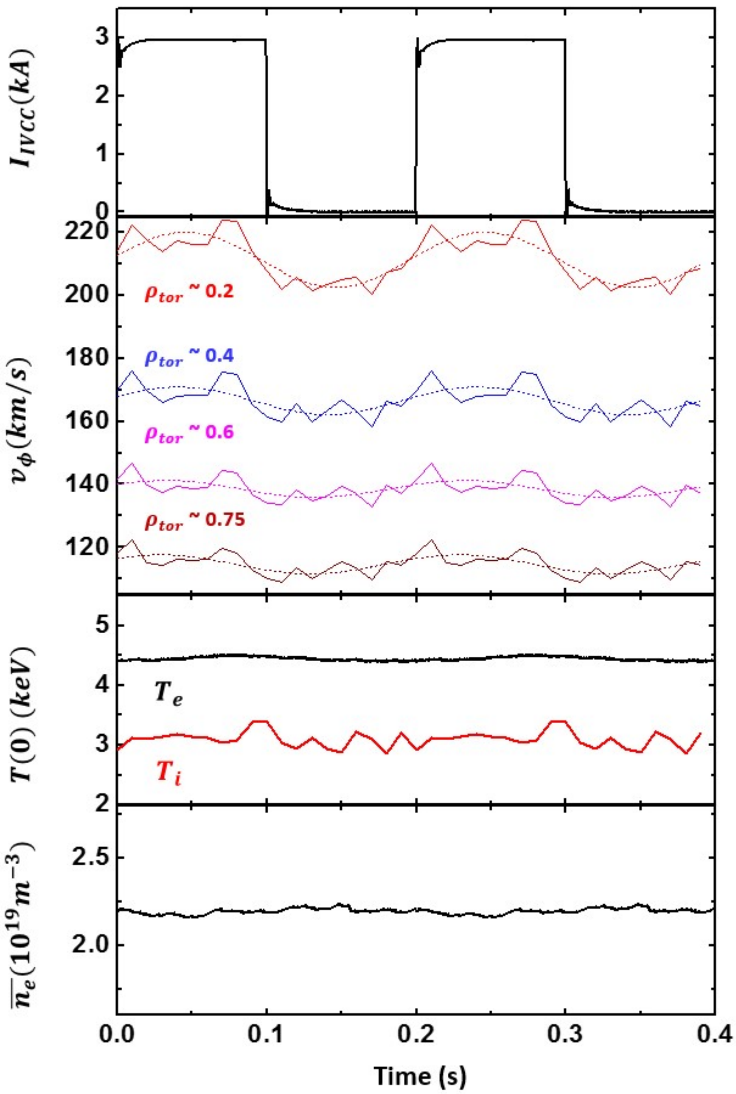

Figure 3.6 Time traces of the conditional averaged I_{IVCC}, v_ϕ, T_i, T_e, and $\bar{n}_e$ for the KSTAR NRMP modulation experiment (#13650).

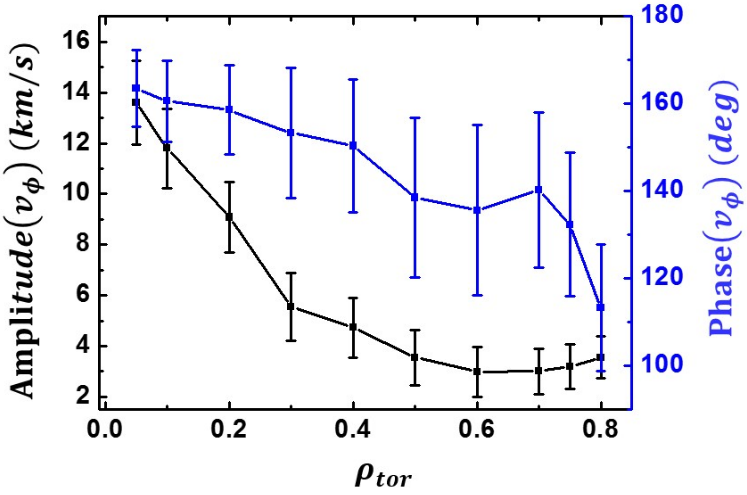

Figure 3.7 Radial profiles of the experimental amplitude and phase of the v_ϕ modulation at 5 Hz in the KSTAR NRMP modulation experiment (#13650).

ment, the effect is less clear than the NBI modulation case, due to the signal noise. In order to separate the possible noise of the edge localized mode (ELM) and other uncertainties, the conditional average is taken during the modulation cycle. Nine modulation cycles are integrated from (5.3 to 7.1) s based on the modulation frequency of $f_{mod} = 5$ Hz. Two identical modulations are plotted in Fig. 3.6 from (0 to 0.2) s and from (0.2 to 0.4) s to see the periodicity of modulations. According to Fig. 3.6, modulated v_ϕ with $f_{mod} = 5$ Hz is clearly identified, while modulations in $T_i(0)$, $T_e(0)$ and $\bar{n}_e$ are not observed. This demonstrates the non-resonant properties of the NRMP modulation in this experiment. One interesting feature in Fig. 3.6 is that the increase of I_{IVCC} does not seem to be directly related to the decrease in v_ϕ, though I_{IVCC} is expected to act as a momentum sink. This can be understood by looking at the time evolution of v_ϕ at various radial positions as shown in Fig. 3.6. When fitted as a sinusoidal wave form, the edge braking is shown to penetrate into the core, when NRMP is applied with a certain time delay. From the NTV analysis elaborated in Sec. 4, we found that this propagation seems to be related to the transport process. Figure 3.7 shows the radial profiles of the experimental amplitude and phase of the v_ϕ modulation at 5 Hz using FFT. The phase values are calculated with respect to the phase of the IVCC current. The IVCC current is considered to have a negative value when it is turned on, since the positive IVCC current acts as a momentum sink. The radial profile of the phase in v_ϕ from the FFT analysis is strongly peaked, and this can explain the penetration of the rotation braking shown in Fig. 3.6. Radial profiles of the amplitude in v_ϕ are relatively peaked around ρ_{tor} =0.2-0.4, which is similar to the result in the previous NBI modulation case. As expected, FFT of T_i in Fig. 3.5 shows no modulation behavior of T_i.

3.3.3 Transport analysis of toroidal rotation using ASTRA

Previous studies adapted the time-dependent transport simulations for the transport analysis of perturbative experiments [33, 34, 42]. One of the important steps for these time-dependent simulations is numerical calculations of the power and torque sources from actuators. In this work, the NBI driven torque is calculated with the NUBEAM [46] code in time-dependent simulations. NUBEAM is a widely used Monte Carlo package for evaluation of the deposition, slowing down, and thermalization of fast ion species in tokamaks. The number of particles used is 150,000, which shows the convergence in the torque calculations. Figure 3.8 shows the resulting torque profiles, where two profiles at different time slices in Fig. 3.3 are plotted to see the change of the torque density profile during the NBI modulation. As expected, the torque profile of NBI is rather broad, in spite of some numerical uncertainties near the magnetic axis.

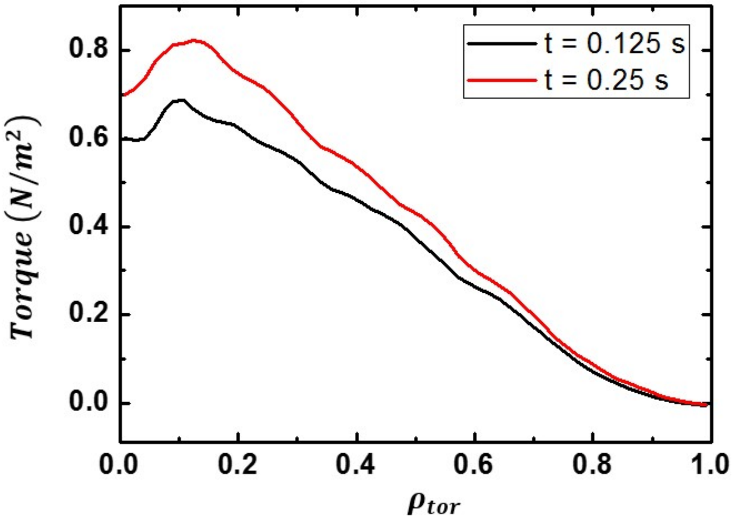

Figure 3.8 Radial profiles of the calculated NBI driven torque density using NUBEAM at the lowest beam power (t = 0.125 s, black), and at the highest beam power (t = 0.245 s, red), during NBI modulation in shot 13652.

The NTV torque is calculated with the IPEC-PENT code [47]. In order to calculate the theoretical torques, the ideal perturbed equilibrium code (IPEC) [23] considering the ideal MHD plasma response from NRMP is used to obtain the non-axisymmetric variation in the field strength. Then, a combined NTV formulation [44] considering the bounce-harmonic resonances with an effective collisional operator is used to calculate the flux-averaged toroidal torque profiles. Since the bounce-harmonic resonance could have an important effect in KSTAR experiments using $n = 1$ NRMP [45], the combined NTV formulation is applied in this study to capture the NTV physics well in KSTAR. Figure 3.9 shows the calculated NTV torque profile from IPEC-PENT. The torque seems to be strongly localized at the edge. This can be explained by the resonance effect, when the bounce-averaged cross drift frequency of ions, which is

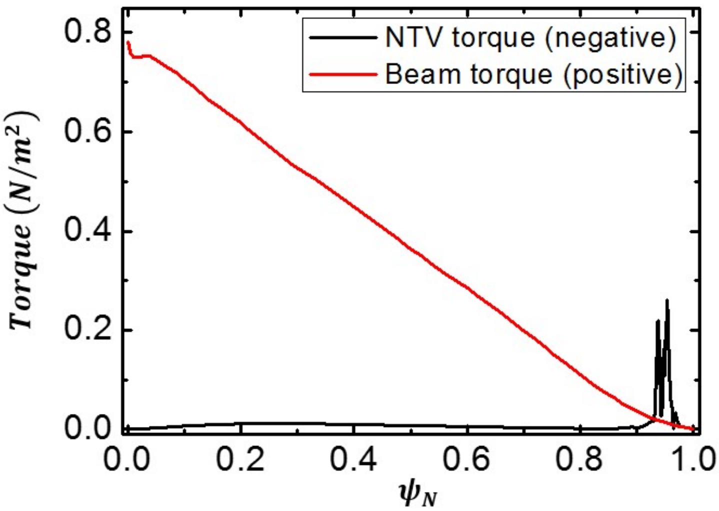

Figure 3.9 Stationary radial profiles of the calculated torque density of NBI (red) by NUBEAM, and the torque density of NRMP (black) by IPEC-PENT, in the NRMP modulation experiment (#13650).

approximated by $E \times B_0$ drift frequency, $\omega_{E\times B} \sim 0$ is satisfied by the strong diamagnetic rotation near the pedestal region. This could explain the experimental behavior shown in Fig. 3.6, that the rotation perturbation propagates from the edge to the core by the transport process. Figure 3.9 shows that although NTV torque in the core also exists, they are much smaller than the background NBI torque. The estimated NTV torque in the core is too small in this discharge and does not have an impact on the phase delay even if there is a time delay in the NTV sink.

The time-dependent transport simulation of the toroidal rotation is carried out using the ASTRA [48] transport code. The transport equation of the angular momentum density, Eq. (3.1) is solved while T_i and T_e are frozen to the experimental values. The n_e profiles are reconstructed using the line-averaged density measurement with the assumption of $n_e\ (\rho_\psi = 0.4)/n_e\ (\rho_\psi = 0.8) \sim 1.3$, based on the measurement with the similar line-averaged density in the other KSTAR H-mode discharge, since the profile measurement was not available in these discharges. As the variation of $\bar{n}_e$ during the modulation is small, we assume that the peaking of n_e does not change in the momentum transport analysis. The boundary condition for the angular momentum density is chosen to fit the amplitudes and phases of modulated v_ϕ at $\rho_{tor} = 0.75$. The edge plasma transport outside this position is beyond the scope of this study. Here, the residual stress driven torque in the core is assumed to be negligible. Note that the residual stress near the pedestal region will not affect the analysis, since the boundary condition $\rho_{tor} = 0.75$ covers the information of the pedestal. The time-dependent transport simulations are carried out in the following steps. First, the interpretative simulation is performed to calculate χ_i. Then, matching of the experimental phase profile is attempted by scanning P_r in predictive simulations. The P_r value is varied, until reasonable reproduction of the experimental phase profile of the modulated v_ϕ is obtained. In these simulations, the phase is mostly determined by χ_ϕ. This is because χ_ϕ is related to the highest spatial derivative which can propagate faster. As the next step, the RV_{pinch}/χ_ϕ value is varied to reproduce the amplitude of the modulated v_ϕ and its stationary profiles. From these results, we could find that inclusion of pinch can better match the experimental phase, amplitude profiles within the error bar as shown in Fig. 3.10 and 3.11. Figure 3.12 shows the determined χ_ϕ and V_{pinch} profiles for the NBI modulation case.

The identical steps are carried out for the NRMP modulation case, except for the torque calculation conducted with IPEC-PENT. Although both the NTV torque and the pedestal are located at the edge, $\rho_{tor} > 0.75$, the edge rotation at $\rho_{tor} = 0.75$ is used as a boundary condition for the momentum transport study. This means we treat the rotation variation at the boundary as the origin of momentum transport. There could be other unknown effects driven by NRMP, though NTV modelling is known to explain this braking effect. So, we have investigated the sensitivity of the NTV torque, by artificially increasing the modelled torque by 10 times. This does not have strong effect on our analysis due to its very small torque in the core region. This uncertainty might explain some undesired result appeared in figure 3.11 where we could find including the pinch effect still cannot fit the amplitude profiles near the magnetic axis $\rho_{tor} < 0.3$, though it works better than the diffusivity only case. Still, it could match the amplitude profiles near the transport region, around $0.3 < \rho_{tor} < 0.75$. So, our study focuses on this region for the comparison with the NBI case. Also, previous studies [35, 36, 38] used only the NRMP-off time for momentum transport analysis, to avoid uncertainties in the NTV torque. Note that the simulations can match the time traces of v_ϕ during both NRMP-on and -off time; this means the calculated χ_ϕ and V_{pinch} profiles could

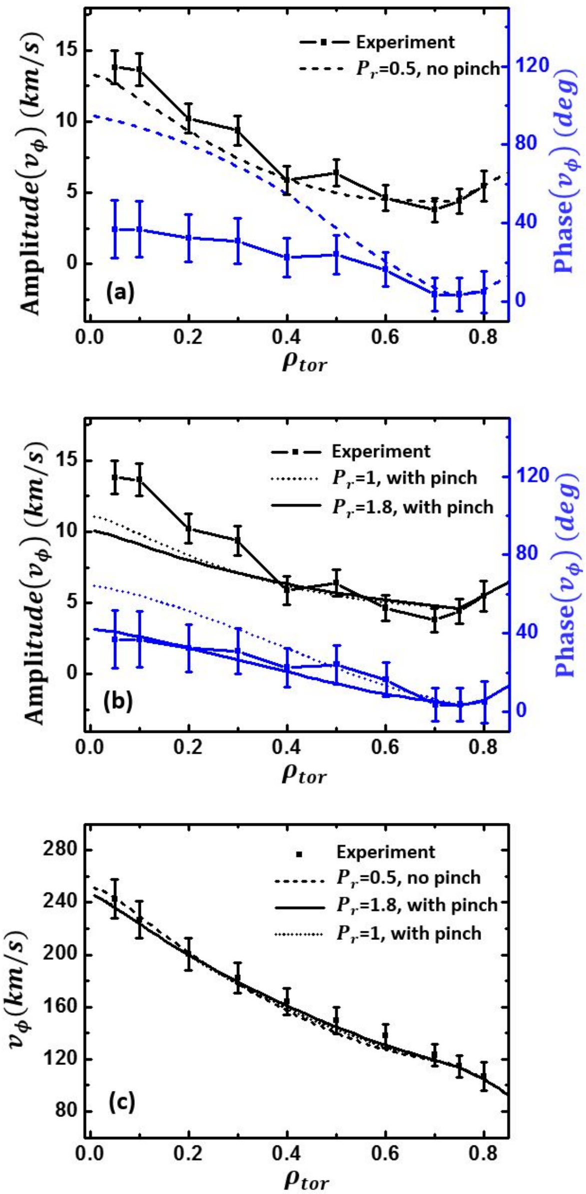

Figure 3.10 (a) Radial profiles of the experimental and the simulated amplitude and phase of v_ϕ in shot 13652 with $P_r \sim 0.5$ and $V_{pinch} = 0$. (b) Radial profiles of the experimental and the simulated amplitude and phase of v_ϕ in shot 13652 with $P_r \sim 1$ and 1.8 with V_{pinch}. (c) The radial profiles of the experimental and the simulated toroidal rotation using two different sets of transport coefficients are shown.

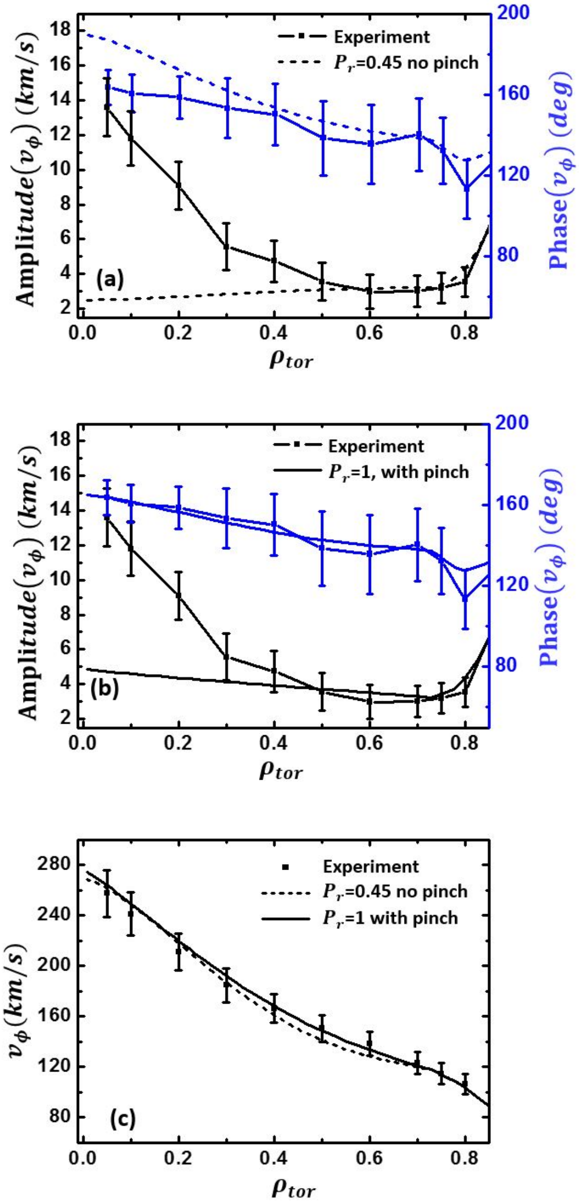

Figure 3.11 (a) Radial profiles of the experimental and the simulated amplitude and phase of v_ϕ in shot 13650 with $P_r \sim 0.45$ and $V_{pinch} = 0$. (b) Radial profiles of the experimental and the simulated amplitude and phase of v_ϕ in shot 13650 with $P_r \sim 1$ and V_{pinch}. (c) The radial profiles of the experimental and the simulated toroidal rotation using two different sets of transport coefficients are shown.

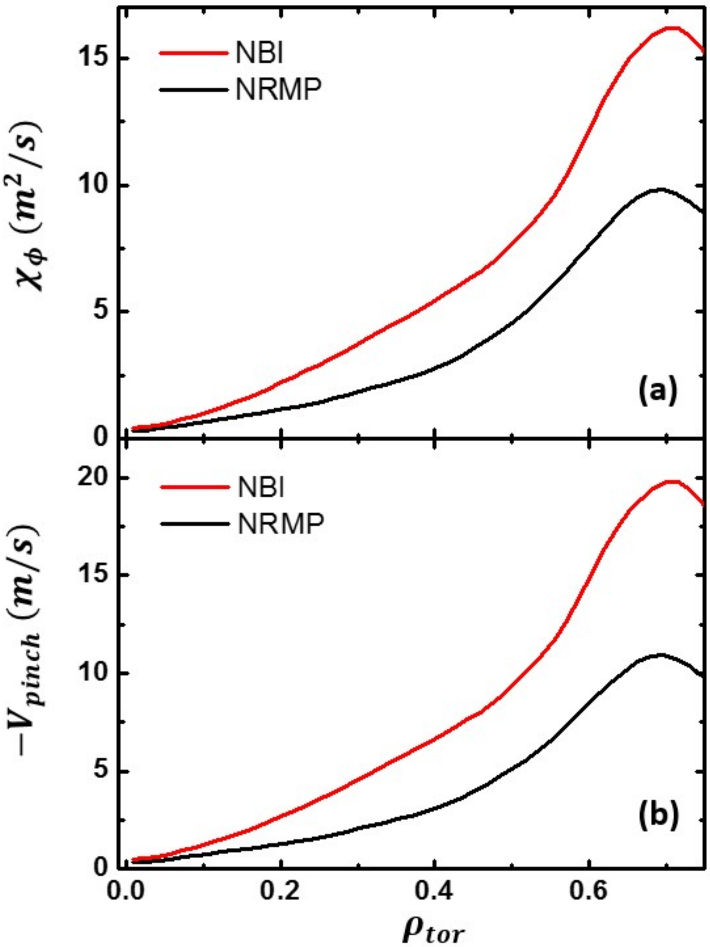

Figure 3.12 Radial profiles of (a) χ_ϕ and (b) V_{pinch} determined from the time-dependent simulations of the NBI modulation experiment (#13652, red), and the NRMP modulation experiment (#13650, black) with the time constant momentum diffusivity.

be reasonable, even with some uncertainties in the NTV torque calculation. Figure 3.12 (b) shows the calculated χ_ϕ and V_{pinch} profiles in the NRMP case. Note that the analysis is done for $\rho_{tor} > 0.3$, by considering the uncertainties near the magnetic axis.

3.3.4 Comparison of the transport coefficient

Figures 3.12 (a) and (b) show that the momentum transport properties obtained from the time-dependent transport simulations reveal clear discrepancy between the NBI and the NRMP modulation experiment. Analyses show that the momentum diffusivity from the NBI modulation experiment is much higher than that from the NRMP modulation experiment. Also, the momentum pinch term is shown to be higher in the NBI modulation experiment than the NRMP one. Note that the two dedicated experiments are designed to operate in the similar plasma condition, so to have similar heating power, plasma current, toroidal magnetic field, and plasma shape at $q_{95} \sim 8$. As a result, the two discharges have similar line-averaged density, $\bar{n}_e = 2.1 \times 10^{19} m^{-3}$ and $\bar{n}_e = 2.2 \times 10^{19} m^{-3}$ and total stored energy ($W_{dia} = 250$ and $W_{dia} = 230$ kJ), in the NBI modulation experiment and the NRMP modulation experiments, respectively. Figures 3.13 (a) and (b) show the radial profiles of the ion temperature and the toroidal rotation averaged over the modulation cycles. These show that the T_i profiles are similar, with small differences between the two discharges. Figure 3.13 (c) shows similar ion heat diffusivity profiles in the two cases, where the injected heating powers are similar. Figure 3.13 (b) shows that there are few differences between the two cases in the toroidal rotation profile

Therefore, it is reasonable to consider that there are no significant differences in the plasma condition between the two cases. The largest differences in the two

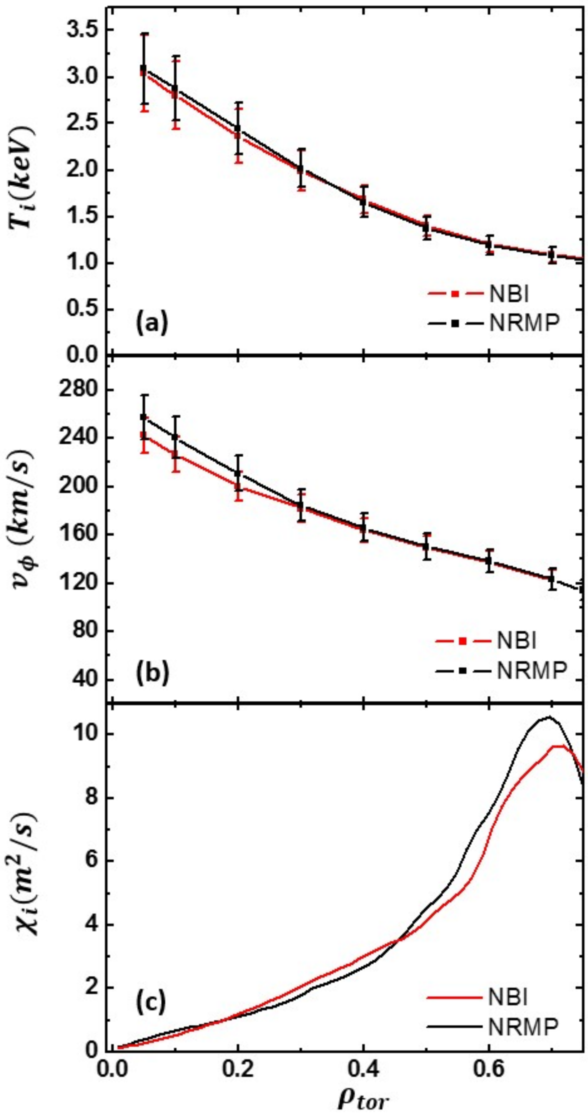

Figure 3.13 Time averaged radial profiles during the modulation period T_i (a), v_ϕ (b), and (c) ion heat diffusivity in the NRMP and the NBI modulation experiment.

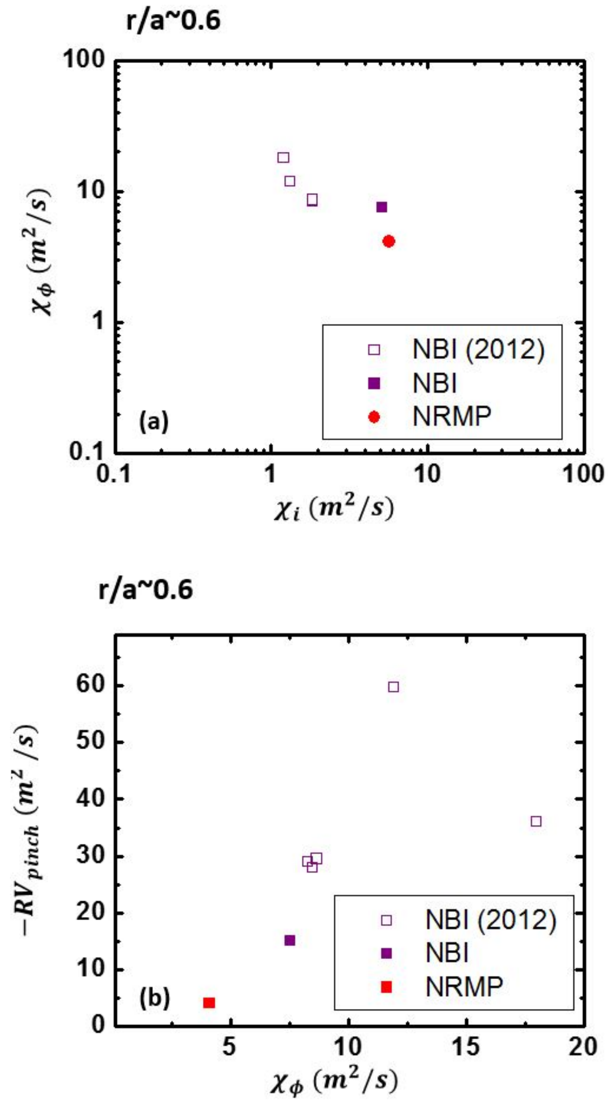

Figure 3.14 Correlation between χ_ϕ and χ_i at $r/a \sim 0.6$ in the KSTAR H-mode experiments. The difference in symbol/color corresponds to the different actuators used for the perturbative analysis; NBI modulation (square/violet) and NRMP modulation (circle/red), respectively. Shot 13652 is indicated as closed violet square, and the other H-mode shots as open violet squares. Note that their experimental conditions are different.

discharges occur in the amplitude of the ion temperature perturbation, as shown in Fig. 3.5. This could be understood as a property of each actuator, since the tangential NBI delivers plasma heating in addition to the toroidal torque by the collisional process, while NRMP applies the torque only by the non-ambipolar transport with the non-resonant field spectrum. Interestingly, this actuator dependence could be found in the result of a previous multi-machine comparison study [39]. Analyses in JET and JT-60U usually give $P_r > 1$ at r/a ~ 0.6 in the perturbative experiments where NBI is used as actuator. Theoretically, when the intrinsic rotation feeds back on itself and renormalizes the momentum diffusivity, $P_r > 1$ can be possible [26]. In contrast, the other tokamaks exhibit $P_r < 1$ where other actuators are used, such as NRMP, NBI-blip, or L-H transition. Gyrokinetic particle-in-cell code showed the theoretical possibility of the estimated $P_r < 1$, when the wave-particle resonance energy is larger than the thermal energy [49]. Additional KSTAR H-modes experiments in 2012 also show a similar trend of $P_r > 1$ from NBI modulation experiments, as shown in Fig. 3.14 (a) (open squares). The absolute value of $-RV_{pinch}$ obtained from the NBI modulation experiments is also larger than that from the NRMP modulation experiments, as shown in Fig. 3.14 (b). The additional experiments are carried out with various f_{mod} = (4, 5, 10) Hz but the ion temperature perturbation clearly exists in all discharges as in shot 13652. Although experimental uncertainty could exist, it is interesting to see that $P_r > 1$ is obtained in all the NBI modulation experiments, while $P_r < 1$ is obtained in the NRMP modulation experiment in KSTAR.

To compare this result with the gyrokinetic theory, a linear gyrokinetic analysis is performed using GKW [50] at r/a=0.6 in the typical experimental condition of shots 13652 and 13650 as shown in Fig. 3.15. Simulations are based on the real geometries based on the CHEASE [51] equilibrium reconstruction.

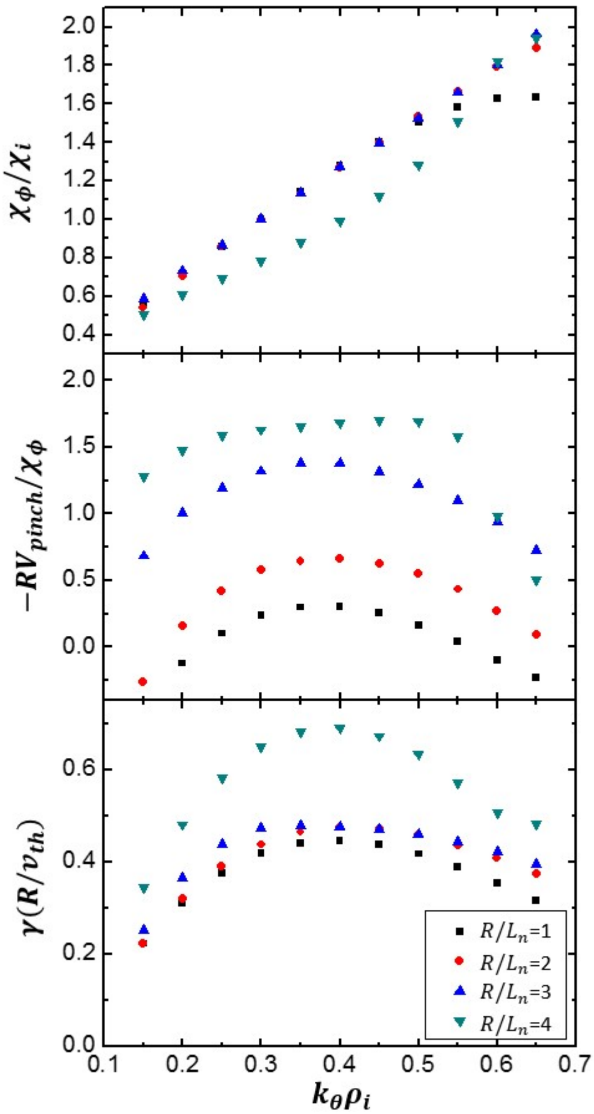

Figure 3.15 Prandtl number, pinch number, and linear growth rate simulated with GKW at $r/a \sim 0.6$.

Since the density gradients are not directly measured in the discharges, we have investigated various density gradients based on the measurement with the similar line-averaged density in other KSTAR H-modes. $P_r \simeq 1 \sim 1.2$ is observed in the simulation around its maximum growth rate, where their values are sensitive to $k_\theta \rho_i$. Pinch numbers could range from around 0.5 to 2 depending more on the density gradients. In order to understand the difference between the NBI and the NRMP modulation experiment, the potential effect of the ion temperature perturbation driven by the NBI modulation to the perturbative analysis is investigated in the following sections. Since the ion heat transport is known to be coupled to the momentum transport, the ion temperature perturbation is expected to affect the result of the perturbative momentum transport analysis.

3.4 Effect of ion temperature perturbation

3.4.1 Effect of the T_i perturbation in linearized equation

A possible effect of the modulated ion temperature to momentum diffusivity in the perturbative analysis is discussed in this section. The modulated ion temperature perturbation driven by the NBI modulation induces a periodic change of the plasma parameters, especially on R/L_{T_i}. The change of R/L_{T_i} could result in strongly enhanced ion heat fluxes based on the critical gradient transport theory with ITG turbulence. The critical gradient model can be demonstrated as [52]:

$$\chi_T = \chi_{gB}\left[\chi_s\left(R/L_{Ti} - R/L_{Ti,crit}\right) H\left(R/L_{Ti} - R/L_{Ti,crit}\right) + \chi_0\right] \tag{3.2}$$

where, $\chi_{gB} = q^{1.5}(T/eB)\rho_s/R$. Here, χ_s characterizes stiffness, $R/L_{Ti,crit}$ is the instability threshold, and $H(x)$ is the Heaviside function. χ_0 is a finite diffusivity below the threshold. Equation (3.2) indicates that if R/L_{Ti} reaches its threshold, $R/L_{Ti,crit}$, the diffusivity can increase abruptly. In addition to χ_i, the property of χ_ϕ could be interpreted to have these critical gradient properties driven by R/L_{Ti}. This is possibly due to the strong coupling between the ion heat transport and the momentum transport since both are caused mainly by the electrostatic micro-turbulence such as the ion temperature gradient (ITG) instability [53]. Various literatures support this strong coupling represented by P_r [54–56]. This strong coupling means that an increase in R/L_{Ti} could eventually lead to the increase of the momentum flux in addition to the ion heat flux, without causing too much change in P_r.

The χ_i and χ_ϕ change during the T_i modulation is around $\pm 10\%$ in the experiment, which seems to be not large to explain the discrepancy in Fig. 3.14. However, the propagation of the perturbed quantity used in the perturbative analysis could be significantly affected by this variation which could to be understood with the linearized angular momentum density equation. The linearized equation of the perturbed angular momentum flux starting from Eq. (3.1) is written as Eq. (3.3), retaining the dependence of ∇T_i, T_i ∇v_ϕ, and v_ϕ, the perturbed quantity from the NBI modulated experiments.

$$\begin{aligned}\tilde{\Pi}_\phi = &- nmR\chi_\phi \frac{\partial \tilde{v}_\phi}{\partial x} + nmRV_{pinch}\tilde{v}_\phi + \tilde{\Pi}_{res} \\ &- \left(\nabla \tilde{v}_\phi \frac{\partial \chi_\phi}{\partial \nabla v_\phi} + \tilde{v}_\phi \frac{\partial \chi_\phi}{\partial v_\phi} + \nabla \tilde{T}_i \frac{\partial \chi_\phi}{\partial \nabla T_i} + \tilde{T}_i \frac{\partial \chi_\phi}{\partial T_i} \right) nmR \frac{\partial v_{\phi 0}}{\partial x} \\ &+ \left(\nabla \tilde{v}_\phi \frac{\partial V_{pinch}}{\partial \nabla v_\phi} + \tilde{v}_\phi \frac{\partial V_{pinch}}{\partial v_\phi} + \nabla \tilde{T}_i \frac{\partial V_{pinch}}{\partial \nabla T_i} + \tilde{T}_i \frac{\partial V_{pinch}}{\partial T_i} \right) nmRv_{\phi 0}\end{aligned} \tag{3.3}$$

In addition to the first three terms in Right Hand Side (RHS) of Eq. (3.3), extra contributions could exist, if thermodynamic dependences are retained. Although the change of ∇v_ϕcould drive an additional dependence by ExB shearing, the change in ∇v_ϕ exists in both the NRMP and the NBI modulation experiment. Note that since the main purpose of this section is to find differences in analysis using NRMP and NBI, the T_i perturbation-driven effects are our only interest, and are considered in this section for simplicity. We also assumed fast perturbation, where only the highest spatial derivatives need be considered. The assumption of this fast perturbation could be applied for 4 Hz, our modulated frequency in the experiment, based on the result of predictive simulations in Sec. 4. The linearized equation of the perturbed angular momentum conservation for demonstrating the fast perturbation can be given, retaining the functional dependences, by:

$$nmR\frac{\partial \tilde{v}_\phi}{\partial t} = nmR\chi_\phi \frac{\partial^2 \tilde{v}_\phi}{\partial x^2} + \left(nmR\frac{\partial \chi_\phi}{\partial \nabla T_i}\frac{\partial v_{\phi 0}}{\partial x} - nmR\frac{\partial V_{pinch}}{\partial \nabla T_i} v_{\phi 0} \right) \frac{\partial \tilde{T}_i}{\partial x^2} + \tilde{S}. \tag{3.4}$$

Here, $\tilde{\Pi}_{res}$ is ignored in angular momentum conservation equation by the relation $\nabla \cdot \Pi_{res} \propto \nabla T_i$ [57], since it only depends on the first derivate ∇T_i. It is clear that the fast perturbation of the perturbed momentum flux must be described by adding the 2nd term in the RHS of Eq. (3.4), which becomes more important with the larger ion temperature perturbation. Constraining the relation between T_i and v_ϕ driven by the actuator, Eq. (3.4) may be written as:

$$\begin{aligned} nmR\frac{\partial \tilde{v}_\phi}{\partial t} =& nmR\chi_\phi \frac{\partial^2 \tilde{v}_\phi}{\partial x^2} + \tilde{S} \\ &+ \left(\left(\frac{\partial \chi_\phi}{\partial \nabla T_i}\frac{\partial v_{\phi 0}}{\partial x} - \frac{\partial V_{pinch}}{\partial \nabla T_i} v_{\phi 0} \right) \frac{\partial \tilde{T}_i}{\partial \tilde{v}_\phi}\Big|_{actuator} \right) nmR\frac{\partial^2 \tilde{v}_\phi}{\partial x^2}. \end{aligned} \tag{3.5}$$

We can define χ_ϕ^{pert}, the momentum diffusivity obtained from the radial profile of the phase using the perturbative analysis, as Eq. (3.6):

$$\chi_\phi^{pert} = \chi_\phi + \left(\frac{\partial \chi_\phi}{\partial \nabla T_i}\frac{\partial v_{\phi 0}}{\partial x} - \frac{\partial V_{pinch}}{\partial \nabla T_i} v_{\phi 0} \right) \frac{\partial \tilde{T}_i}{\partial \tilde{v}_\phi}\Big|_{actuator} \tag{3.6}$$

The second term in the RHS of Eq. (3.6) demonstrates the difference between χ_ϕ^{pert} in Eq. (3.6), and χ_ϕ in Eq. (3.1). If there is no T_i modulation, $\frac{\partial \tilde{T}_i}{\partial \tilde{v}_\phi}$ can be ignored, so that χ_ϕ^{pert} becomes identical to χ_ϕ, which is the case of the NRMP modulation experiment. However, in the NBI modulation case, positive values of $\frac{\partial \tilde{T}_i}{\partial \tilde{v}_\phi}$ are expected, since NBI induces the increase of both T_i and v_ϕ for the co-injection case. Based on Eq. (3.3) and (3.6), we could obtain Eq. (3.7) by considering a time constant P_r and $\alpha_{pinch} = RV_{pinch}/\chi_\phi$ during the modulation. We also assumed that the neoclassical diffusivity is small, and the critical gradient $R/L_{Ti,crit}$ is reached, so that the transport is governed by the turbulent transport in the experiment. Concerning that $\nabla v_{\phi 0} > v_{\phi 0}$, Eq. (3.6) becomes

$$\chi_\phi^{pert} = \chi_\phi \left(1 + \frac{\nabla v_{\phi 0}}{\nabla T_i - \nabla T_{i,crit}} \frac{\partial \tilde{T}_i}{\partial \tilde{v}_\phi}\Big|_{actuator} \right) \tag{3.7}$$

The terms related to the actuator in Eq. (3.7) are calculated using the experimental data in the KSTAR NBI modulation experiment. Typically, they are of the order of unity, but they highly depend on the propagation of $\tilde{T}_i$ and $\tilde{v}_\phi$. So, detailed calculations are given with time-dependent transport simulations in the following section. The second term in Eq. (3.7) is positive, when positive is considered as in our NBI experiment. Therefore, the higher level of χ_ϕ^{pert} could be interpreted as a natural consequence of the perturbative analysis with a T_i modulation. This could explain the qualitative result of Section 5.1 that the NBI modulation experiments generally show higher momentum diffusivities than the NRMP modulation experiments, since $\chi_\phi^{pert} = \chi_\phi$ is assumed in the previous analysis by time constant χ_ϕ. It is also interesting to note that these additional terms are all driven by the relation $\frac{\partial \tilde{T}_i}{\partial \tilde{v}_\phi}$, and this term survives, even when $\tilde{T}_i$ is small, as long as$\tilde{v}_\phi$ is small during the NBI modulation. Therefore, estimation of higher χ_ϕ in the NBI modulation experiments could be related to the actuator property where both T_i and v_ϕ modulations are triggered from the collisional process, and this should be properly taken into account for the estimation of χ_ϕ.

3.4.2 Effect of the T_i perturbation in transport simulation

This section considers the ion temperature perturbation effects in time-dependent transport simulations that are separated into two parts. The first part deals with the variations of χ_ϕ and V_{pinch} driven by the ion temperature perturbation in the transport simulations, while the later part briefly discusses the effect of the time-varying residual stress. The thermodynamic dependence of χ_ϕ and V_{pinch} results in time-varying χ_ϕ and V_{pinch} under T_i modulation. A pure χ_ϕ variation during the modulation cannot be separated from the stationary rotation profile. Instead, the variation of χ_ϕ can be estimated from the χ_i variation based on the constant P_r assumption. For this, the time evolution of χ_i is calculated based on the time-varying T_i and ion heating power P_i using the power balance analysis. Figure 3.16 (a) shows that the time evolution of T_i is fitted with a sinusoidal waveform, in order to avoid the unrealistic time variation of T_i and $\partial T_i/\partial t$. Based on the calculated heating power shown in Fig. 3.16 (c), a clear modulation of χ_i is estimated as plotted in Fig. 3.16 (d). There are phase differences between χ_i and P_i at $\rho_{tor} = 0.3$. From the time evolution of $\nabla \mathrm{T}_i$ as shown in Fig. 3.16 (b), we could infer that the phase in χ_i at $\rho_{tor} = 0.3$ is dominated by the change in $\nabla \mathrm{T}_i$, while it is dominated by the change in P_i at $\rho_{tor} = 0.6$. The result also shows that during the NBI modulation, χ_i could vary by about 15 %. Under the constant P_r assumption, this implies that the χ_ϕ variation would be around 15 %.

Since the variation of χ_i during the modulation is expected to be non-

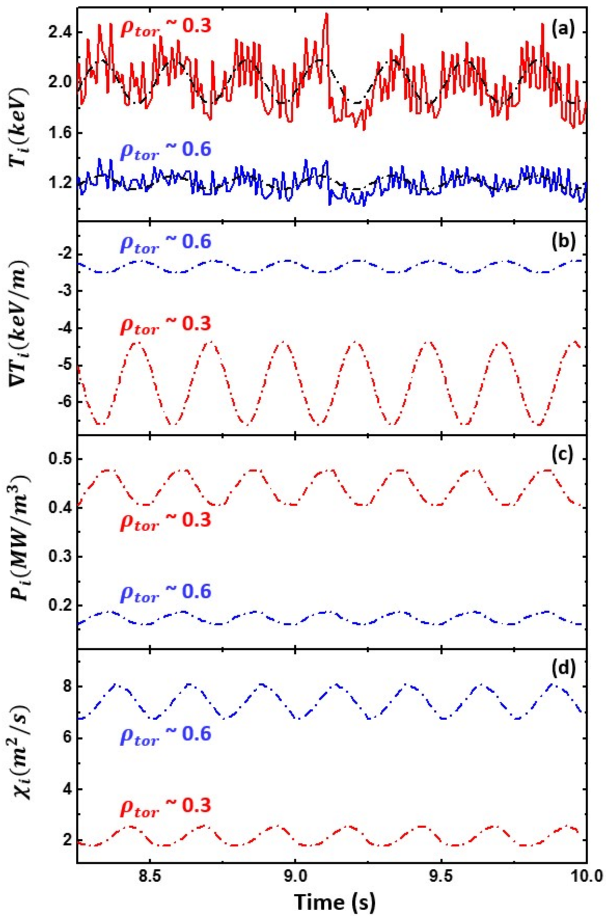

Figure 3.16 (a) Time traces of the measured (solid) and the sine-fitted (dashed) T_i, (b) the ion temperature gradient ∇T_i, (c) the calculated heating power P_i, and (d) the calculated ion heat diffusivity χ_i at $\rho_{tor} = 0.3$ and $\rho_{tor} = 0.6$ for the KSTAR NBI modulation experiment.

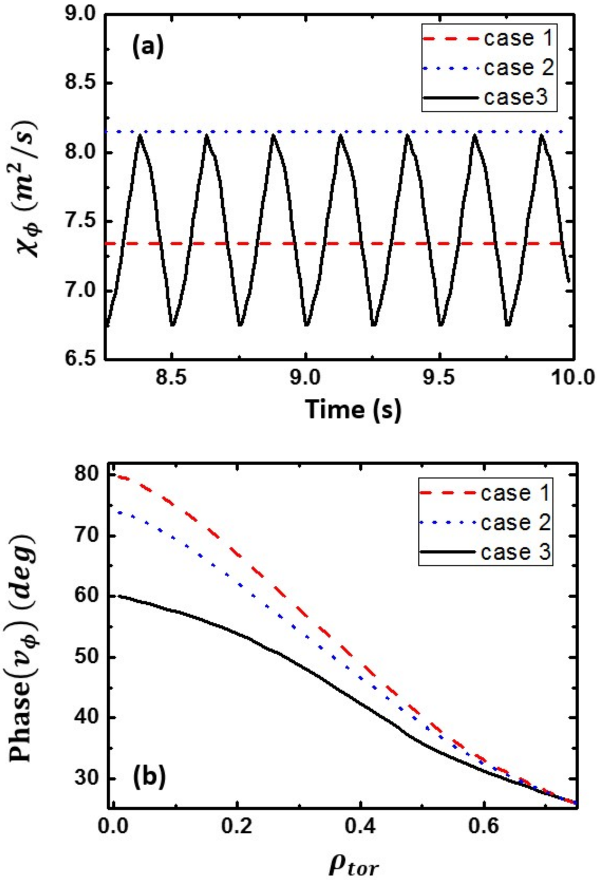

Figure 3.17 (a) Time traces of χ_ϕ prescribed at $\rho_{tor} = 0.6$ for case 1, case 2, and case 3 in transport simulations, and (b) resulting radial profiles of the simulated phase of v_ϕ in each case.

negligible, the possible difference in χ_ϕ^{pert} and χ_ϕ due to the ion temperature perturbation is evaluated with time-dependent transport simulations. Three simple test cases are simulated to compare the time-constant momentum diffusivity and the time-varying momentum diffusivity at $P_r = 1$; case 1 with a mean value of χ_i, case 2 with a maximum value of χ_i, and case 3 with time-varying χ_i during the modulation. Figure 3.17 (a) shows the time traces of χ_ϕ for these three cases at $\rho_{tor} = 0.6$. Figure 3.17 (b) shows the resulting radial profiles of the simulated phase of v_ϕ. By comparing cases 1 and 2, higher momentum diffusivity results in faster propagation of the rotation perturbation, as investigated in the previous section. However, interestingly, the opposite results are found in comparison between cases 2 and 3. Although case 2 has generally higher χ_ϕ than case 3, the propagation of the perturbation in case 3 is shown to be faster. This means that the realistic time variation of χ_ϕ could largely affect the estimated χ_ϕ in the perturbative analysis. This time-varying χ_ϕ due to the modulation of T_i could result in ${\chi_\phi}^{pert} > \chi_\phi$, as estimated in Sec. 5.2.

As the time-varying momentum transport coefficients could play an important role in the perturbative analysis, this possibility should be considered while estimating the momentum transport coefficients. Here, P_r and α_{pinch} are set to stay constant during the simulation for simplicity. Taking into account the time-varying χ_ϕ and V_{pinch} gives a significantly reduced χ_ϕ. Here as well, we could find that inclusion of pinch can better match the experimental phase, amplitude profiles within the error bar as shown in Fig. 3.4.2. Figure 3.4.2 (d) shows the radial profiles of χ_ϕ and V_{pinch} that are obtained. They are clearly smaller than those shown in Fig. 3.10 (a), where χ_ϕ is assumed to be constant. The χ_ϕ at r/a 0.6 in Fig. 3.4.2 (a) shows that χ_ϕ becomes about two times smaller, by considering the variation of both χ_ϕ and V_{pinch}. As a result, the discrepancies in χ_ϕ are much reduced, compared with the NRMP modulation case, though χ_ϕ in

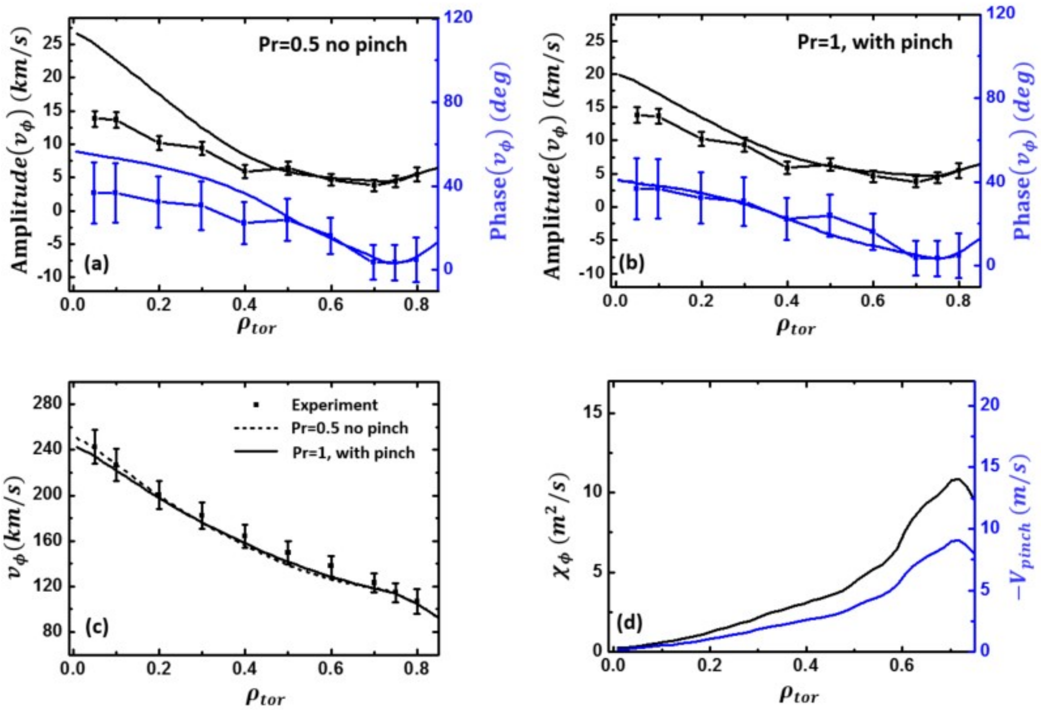

Figure 3.18 (a) Radial profiles of experimental and simulated amplitude and phase of v_ϕ in shot 13652 with $P_r \sim 0.5$ and $V_{pinch} = 0$ with time varying transport coefficients. (b) Radial profiles of experimental and simulated amplitude and phase of v_ϕ in shot 13652 with $P_r \sim 1$ and V_{pinch} with time varying transport coefficients. (c) The radial profiles of the experimental and simulated toroidal rotation using two different transport options are shown. (d) The radial profiles of the experimental and simulated toroidal rotation using two different transport options are shown.

the NBI modulation case is still higher. The V_{pinch} at r/a 0.6 is also reduced, as shown in Fig. 3.4.2 (b). The discrepancy still left in two cases could be related to the assumption of constant P_r and α_{pinch}. Understanding and applying its more realistic time-variation may further reduce the discrepancy.

In addition to time-varying χ_ϕ and V_{pinch}, the ion temperature perturbation could be related to the time-varying residual stress, and could affect the perturbative transport analysis. From the Eq. (3.4), intrinsic torque driven by $\nabla \mathrm{T}_i$ could be neglected in the fast perturbation. However, its effect on the amplitude profile is not negligible, and contributes to the V_{pinch} estimation. So, the intrinsic torque driven by the residual stress needs to be further studied for better estimation of V_{pinch}, and will be clarified in future experiments.

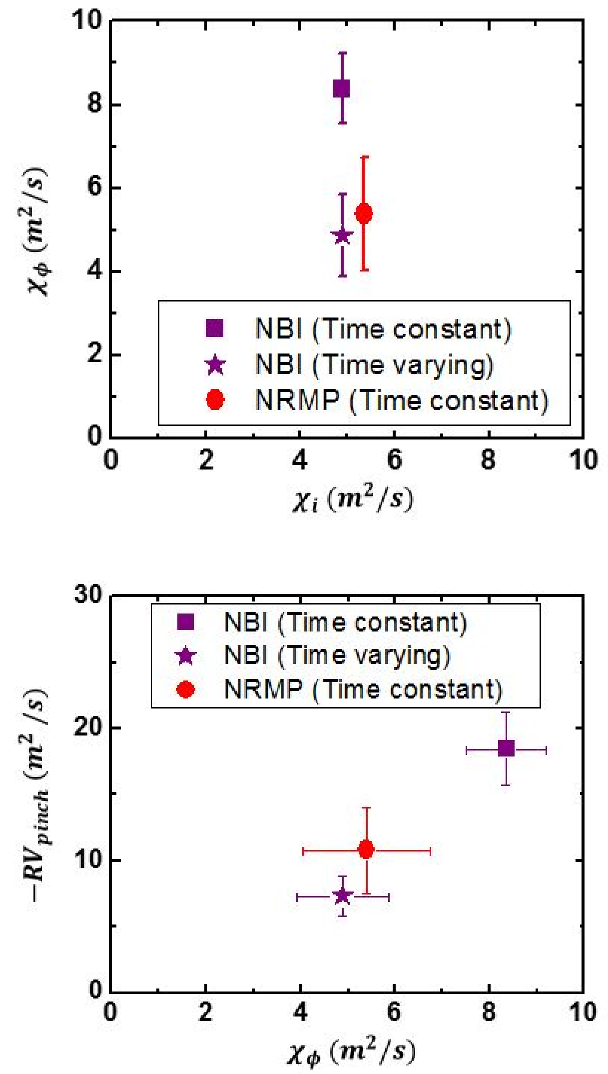

Figure 3.19 Correlation between χ_ϕ and χ_i at $r/a \sim 0.6$, and (b) Correlation between χ_ϕ and V_{pinch} at $r/a \sim 0.6$. The cases with (square) and without (star) considering the time-varying transport coefficients are compared for the NBI modulation experiments. The NRMP modulation case is indicated by red circle.

Chapter 4

Acceleration of plasma rotation by electron non-ambipolar transport

A presence of static non-axisymmetric field usually induces the braking of the plasma rotation. The braking of toroidal rotation may be not favorable of plasma stability and confinement [6–10], while it can still lead to the local increase of rotation shear. Although it is not commonly observable, there are some experimental observations which show that the static 3D fields can accelerate plasma rotation in several devices. In DIIID, acceleration of the plasma rotation in the counter-current direction is observed, and its properties can be explained by ion NTV offset rate [58]. In TEXTOR, acceleration of the rotation in the co-current direction is found, where the accelerations are independent of the NBI heating power and injection torque direction. A formation of the stochastic layer is a strong candidate to explain the result [59]. The accelerations are also found in J-TEXT with a change of the plasma properties near the mode rational surface. The change of the turbulent stress are measured by the Mach probe, and the acceleration is found to be related to the turbulent stress [60]. In this chapter, the acceleration of the plasma rotation by the 3D field in KSTAR is introduced, which shows different properties compared to the previous studies.

4.1 Rotation acceleration by NTV offset

One important effect of the 3D field on plasma rotation is known as NTV [12,43] as introduced in Eq. (1.3). In the presence of 3D non-axisymmetric magnetic fields, particles can radially drift on the perturbed magnetic field line and this process can be interpreted as NTV. The non-ambipolar radial transport rate can be related to the anisotropic tensor term in the momentum balance equation, which can be given by,

$$\left\langle \boldsymbol{e_\phi} \cdot \boldsymbol{\nabla} \cdot \overleftrightarrow{\Pi}_s \right\rangle = q_s \Gamma^{na}, \tag{4.1}$$

where the anisotropic tensor is given by

$$\overleftrightarrow{\Pi}_s = \left(p_{\parallel s} - p_{\perp s}\right)\left(\overrightarrow{bb} - \frac{1}{3}\overleftrightarrow{I}\right). \tag{4.2}$$

The anisotropic pressure can be given by the relation

$$p_\perp - p_\parallel = m \int \left(v_\perp^2/2 - v_\parallel^2\right)\left(f_1 + \cdots\right) d\vec{v}. \tag{4.3}$$

One can approximate the perturbed distribution function f_1 by the deviation of equilibrium distribution function. The f_1 can be calculated from the drift kinetic equation. With a drift kinetic ordering $\rho_g \beta / L$, where ρ_g is the gyro-radius, $\beta \equiv 8\pi p / B^2$ and L is the characteristic length of the variation of the magnetic field, the drift kinetic equation in an equilibrium can be given by

$$\left(\vec{v}_\parallel + \vec{v}_D\right) \cdot \vec{\nabla} f = C\left[f\right]. \tag{4.4}$$

By solving drift kinetic equation in the presence of the 3D field, one can estimate the perturbed distribution function f_1 in the various asymptotic regimes which are reviewed in previous studies [11, 61]. Its solution f_1 generally includes thermodynamic drive term $\frac{\partial f_0}{\partial \psi}$. In the Maxwellian distribution function, $f_0 = f_M$, $\frac{\partial f_M}{\partial \psi}$ can be written as

$$\frac{\partial f_M}{\partial \psi} = -\frac{q f_M}{T_{i0}} \left[\omega_\phi - \omega_{NC0,s}\left(E,\theta\right)\right]. \tag{4.5}$$

For ions, $\omega_{NC0,i}$ can be written as

$$\omega_{NC0,i}\left(E,\theta\right) \equiv \left[c_p \frac{I^2}{R^2 \left\langle B_0^2 \right\rangle} + \left(\frac{E}{T_{i0}} - \frac{5}{2}\right)\right] \frac{1}{e} \frac{\partial T_{i0}}{\partial \psi}, \tag{4.6}$$

and ω_{e0} for electrons can be written as

$$\omega_{NC0,e}\left(E,\theta\right) \equiv \left[c_p \frac{I^2}{R^2 \left\langle B_0^2 \right\rangle} - \frac{1}{e n_{i0}} \frac{\partial p_{i0}}{\partial \psi} - \frac{1}{e n_{e0}} \frac{\partial p_{e0}}{\partial \psi} - \left(\frac{E}{T_{e0}} - \frac{5}{2}\right)\right] \frac{1}{e} \frac{\partial T_{e0}}{\partial \psi}. \tag{4.7}$$

Here, c_p is poloidal rotation coefficient which can be given by neoclassical theory [62]. One can see that there exist a finite level of offset frequency rate, given by ω_{NC0}. The rate represents that NTV will try to relax the plasma to restore ambipolarity to specific rotation level. This can be further represented as so-called neoclassical offset, by taking the flux surface average of Eqs. (4.6) and (4.7), given by

$$\omega_{NC,i} \equiv v_\theta + c_{t,i} \frac{1}{e} \frac{\partial T_{i0}}{\partial \psi}, \tag{4.8}$$

$$\omega_{NC,e} \equiv v_\theta - \frac{1}{n_{e0} e} \frac{\partial p_{e0}}{\partial \psi} - \frac{1}{n_{i0} e} \frac{\partial p_{i0}}{\partial \psi} + c_{t,e} \frac{1}{e} \frac{\partial T_{e0}}{\partial \psi}, \tag{4.9}$$

Two different form Eqs. (4.8) and (4.9) clearly shows that neoclassical offset frequency depends on the particle species. The constant c_t can be given by taking the flux surface average of Eqs. (4.6), (4.7). The integrals are complex, but one can simplify the expression in various asymptotic limits in cylindrical geometry. The various asymptotic regimes can be separated by their collisionality and precession frequency which is reviewed in Ref. [63]. By looking at the Eqs. (4.6), (4.7), one can clearly see the sign dependence in front of the $\frac{\partial T}{\partial \psi}$ term. This clearly shows that the direction of the neoclassical offset rate is opposite for ions and electrons. Typically, the neoclassical offset rate is a counter-current direction for ions while it is a co-current direction for the electrons. The ion NTV offset rate has been validated in DIIID by the rotation acceleration towards counter-current direction [58].

4.2 Co-current acceleration and offset in KSTAR

A co-current offset rotation has been introduced in KSTAR, which can be explained generalized offset rotation around the edge region [64]. The KSTAR experiments introduced in Fig. 4.1 clearly show the global acceleration of toroidal rotation due to a 3D magnetic field, and the saturation of the effect at a particular level of rotation. Here the top trace shows the applied $n = 1$ resonant magnetic field, for which the currents in 3 rows of in-vessel control coils (IVCC) are relatively shifted by 90^o toroidal angle. This 3D setting is often used to generate a resonant magnetic perturbation (RMP) to suppress the edge-localized-mode (ELM) in KSTAR [4]. Here our target plasmas are heated by the co-I_P-directed neutral beam injection (NBI) with the $I_P = 0.6MA$ and the toroidal field $B_T = 2T$, which make the so-called safety factor $q_{95} \approx 5$. Another purpose of the experiments is to study the tolerance of low-torque plasmas against $n = 1$ disruptive 3D MHD instability the so-called a locked mode (LM) [65] during a period before the transition to a high-confinement (H) mode, and therefore NBI

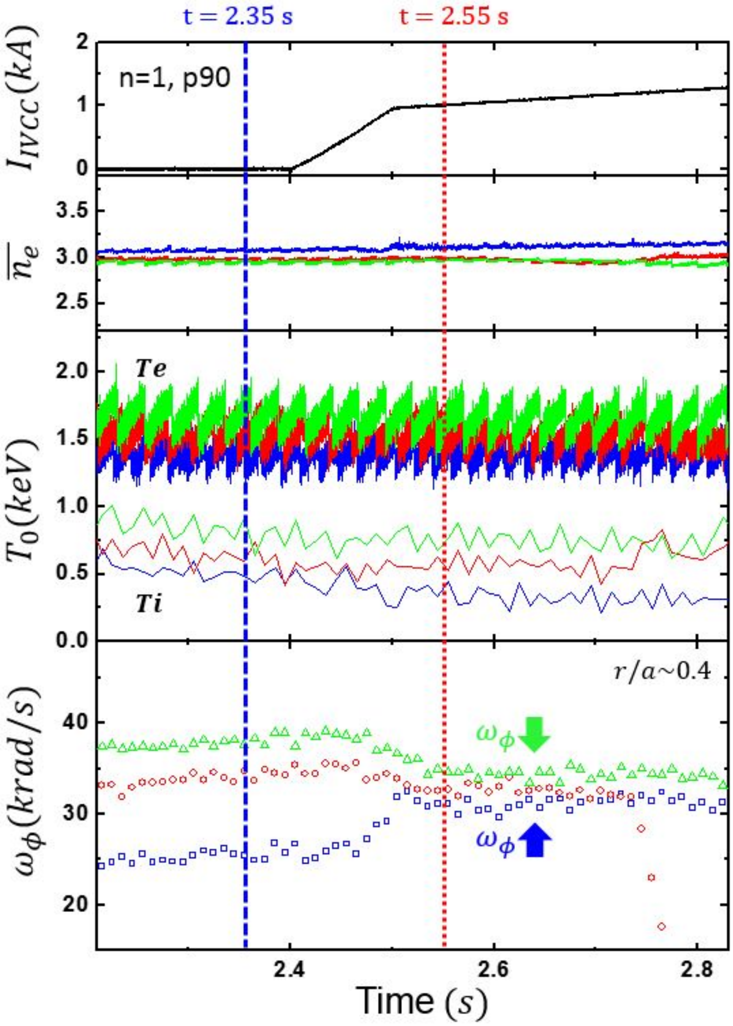

Figure 4.1 The time traces of main plasma parameters in KSTAR discharges. (a) Amplitude of IVCC coil currents, (b) line-averaged plasma density, (c) core electron and ion temperature, (d) toroidal rotation frequency measured at the $r/a \sim 0.4$ location.

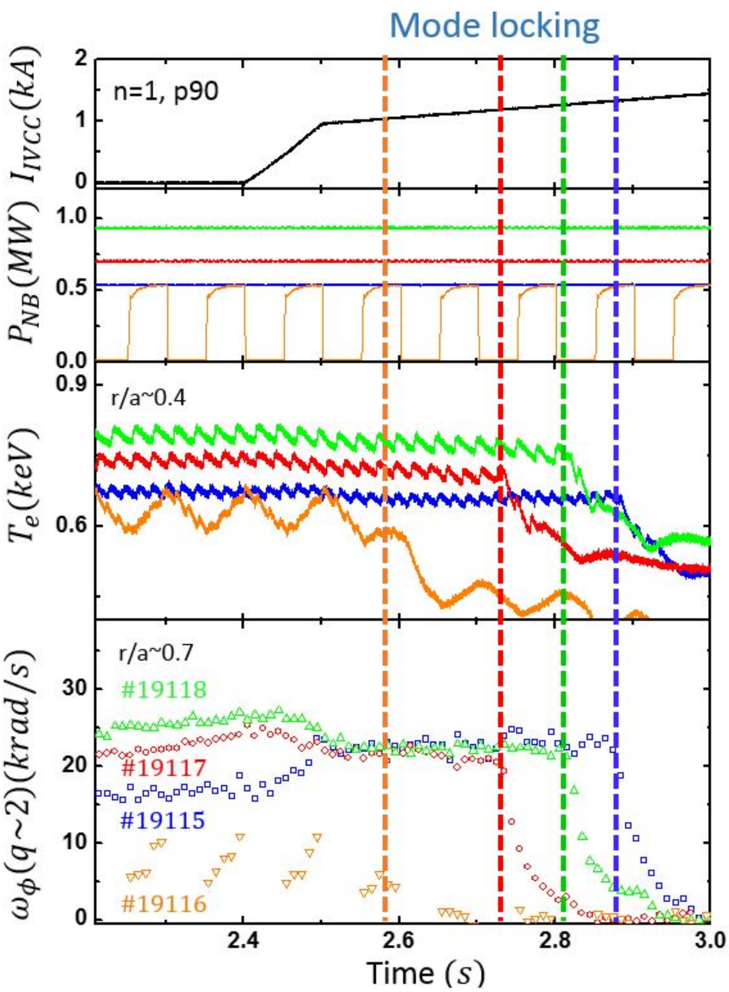

Figure 4.2 The time traces of main plasma parameters in KSTAR discharges. (a) Amplitude of IVCC coil currents, (b) NBI heating power, (c) electron temperature at the $r/a \sim 0.4$, (d) toroidal rotation frequency measured at the $r/a \sim 0.7$ location.

power $P_{NB} < 1MW$ is used and controlled. With the lowest $P_{NB} \sim 0.56MW$ (# 19115), one can see magnetic acceleration of rotation shown in the bottom trace, up to 30% from the core to the edge measured by charges exchange spectroscopy of the carbon impurity [41].

On the other hand, in the faster rotating plasmas in the co-I_P direction, one can see the braking of rotation with the application of $n = 1$ field. Here the second and third traces show that the differences in the line-averaged density, electron temperature (T_e) are within 10 % between all three discharges with the slight differences in the injected NBI power. The plasmas are nearly stationary for all the three discharges even with the applied $n = 1$ resonant magnetic field, except for their rotation approaching the particular level, before the locked mode occurs, which is indicated as vertical dashed lines in Fig. 4.2. After reaching the particular rotation level, the rotation seems to saturate even with a slow increase of n=1 fields before LM. The saturation can be possible when the rotation gets closer to its ambipolar level, as the torque is no longer proportional to the δB^2 [66, 67].

Fig. 4.2 also shows that the magnetic acceleration can improve the tolerance of the low torque plasmas against LM. With the slow increase of the $n = 1$ resonant magnetic field, one can eventually see the sudden decrease of toroidal rotation at the bottom trace. This disruptive MHD event is well known as LM, which occurs with the penetration of the resonant field. There is a local decrease of the toroidal rotation around the $q = 2$ surface during the mode locking in these discharges, which is consistent with the previous studies that the resonant field penetration occurs at the $q = 2$ surface [65]. So, a resonant field to induce the LM is evaluated at the $q = 2$ surface, considering the vacuum and ideal MHD plasma response with the IPEC code [23]. Both calculations showed that #19115, which is rotating slightly faster at the $q = 2$ surface, is more tolerable against LM than other two discharges. The observations are consistent with the previous studies [68, 69], that rotation at the $q = 2$ surface can play a stabilizing effect against the LM. The bottom trace clearly shows that $\omega_\phi\,(q \sim 2)$ eventually becomes higher by magnetic acceleration in #19115, where it initially rotates slower than other discharges before the 3D field is applied. This result clearly shows the feasibility of magnetic acceleration to improve the tolerance of slowly rotating plasmas against the MHD instability. Concerning that observed intrinsic torque of H-mode plasmas is in the co-I_p direction [70], this magnetic acceleration in the co-I_p direction has a potential to maintain the finite plasma rotation in the co-I_p direction.

The magnetic acceleration also leads to the uncommon time evolution of ω_ϕ before the mode locking. Fig. 4.2 shows that the plasma rotation does not decelerate in #19115 until the $n = 1$ field hits the penetration threshold. This shows that toroidal rotation can bifurcate to zero rotation even without a decrease of rotation, unlike the traditional understanding [14, 65]. This is also different from other two discharges which shows that the penetration occurs with the damping of toroidal rotation.

The toroidal rotation frequency before and after 3D field in # 19115 are compared to the neoclassical offset frequency. For estimating the offset rate, the 3D collisionality regime should be evaluated for estimating c_t defined in Eqs. (4.6) and (4.9). After estimating the 3D collisionality regime, one can use the c_t which has been already calculated in the various asymptotic regimes [63]. For estimating the 3D collisionality regime, collision frequency, bounce frequency, and precession frequency should be estimated. A collision frequency can be given by

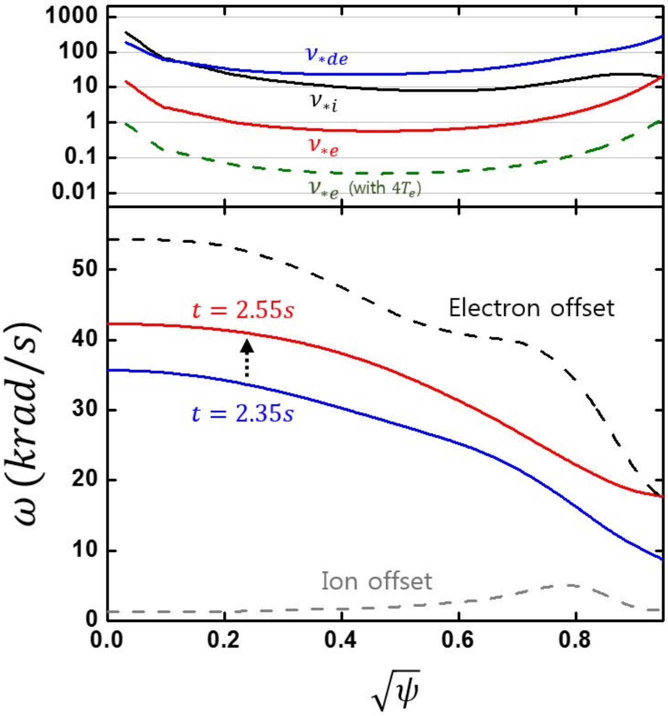

Figure 4.3 (color) (a) Radial profiles of ν_{*i}, ν_{*e}, ν_{*de} for #19115 at t = 2.55 s. (b) Radial profiles of toroidal rotation frequency for #19115 at t = 2.35 s and t = 2.55 s, with electron and ion offset rate at t = 2.55 s.

$$\nu_{Di} = \frac{N_i Z^p_{eff} \ln \Lambda}{3.5 \times 10^{17} \left(\frac{m_i}{m_p}\right)^{1/2} T_i^{3/2} (keV)}, \tag{4.10}$$

where, $x = \left(\frac{v}{v_{thi}}\right)^{1/2}$.

$$Z^p_{eff} = 1 + \frac{\left(\frac{1+A}{2A}\right) Z (Z_{eff} - 1)}{Z - Z_{eff}}, \tag{4.11}$$

with A represents the mass number of the species. It should be noted that Z^p_{eff} is different from the typical Z_{eff} which is defined for the ion pitch angle scattering. The collisionality of electrons can be written as

$$\nu_{De} = \frac{N_e Z_{eff} \ln \Lambda}{3.5 \times 10^{17} \left(\frac{m_e}{m_p}\right)^{1/2} T_e^{3/2} (keV)}, \tag{4.12}$$

which is also written in Ref [71]. Also, the measure of bounce frequency which can be written as

$$\epsilon^{1/2}\omega_t = \left(\frac{r}{R_0}\right)^{1/2} v_{th}/qR_0. \tag{4.13}$$

And transit frequency is given by $\omega_t = v_{th}/qR_0$. $E \times B$ drift frequency can be also written as

$$\omega_E = \frac{d\phi}{d\psi}. \tag{4.14}$$

Based on the plamsa parameters obtained from the experiments, several important parameters which characterizes the NTV damping frequency is calculated in Fig. 4.3 (a) for #19115 at 2.55s. One can see that the deflection of ions would dominate the bounce motion, with $\nu_{*i} \equiv \epsilon^{-3/2}\nu_i/\omega_{bi} > 1$, mainly due to the low ion temperature. On the other hand, the bounce motion of electrons is important unlike ions with $\nu_{*e} < \nu_{*i}$. Although some regions do not satisfy $\nu_{*e} < 1$, there would be a substantial number of electrons finishing the bounce motion in the velocity space. These particles would radially drift by collision rather than precession, with $\nu_{*de} \equiv \nu_e/2\epsilon\omega_E \gg 1$. In this so-called $1/\nu$ regime [12], a non-ambipolar flux can be given as $\Gamma^{na} \propto E^4 e^{E/T_0}$ [11]. From the relation, we found that a dominant contribution for the non-ambipolar flux would come from the 4 times higher energy ($4T_e$) than its thermal energy (T_e). This justifies collsionless NTV regime for electrons for $\sqrt{\psi} < 0.9$, where ψ is the normalized equilibrium poloidal flux. Its offset rate, as given in (4.9), is shown in Fig. 4.3 (b) with $c_{t,e} = 2.4$. Ions are still too collisional even with the approximation, but collision and precession effect cannot be ignored in TTMP [63,72]. Here, we used $c_{t,i} = -0.5$ in Plateau regime for calculating the ion offset rate. Toroidal rotation before ($2.35s$) and after ($2.55s$) 3D field in Fig. 4.3 (b) clearly exhibit that the magnetic acceleration is more relevant to the electron offset rate rather than the ion.

4.3 Estimating NTV torque with numerical simulation

4.3.1 Determination of $\delta\vec{B}$

For estimating NTV torque effect of 3D magnetic perturbation needs to be adequately estimated. The variation of the 3D magnetic field strength can be very different from its vacuum solution, as the plasma response can play a crucial role in determining the $\delta\vec{B}$. There are several examples which show the importance of the plasma response [44], and several response models have been developed to estimate those effects. The MARS-K code [73] is used for this study which solves the linearized ideal single-fluid MHD equations in the non-perturbative approach. Recent studies show the importance of this self-consistent kinetic response [74] using the MARS-K code, and we also calculated with a resistive

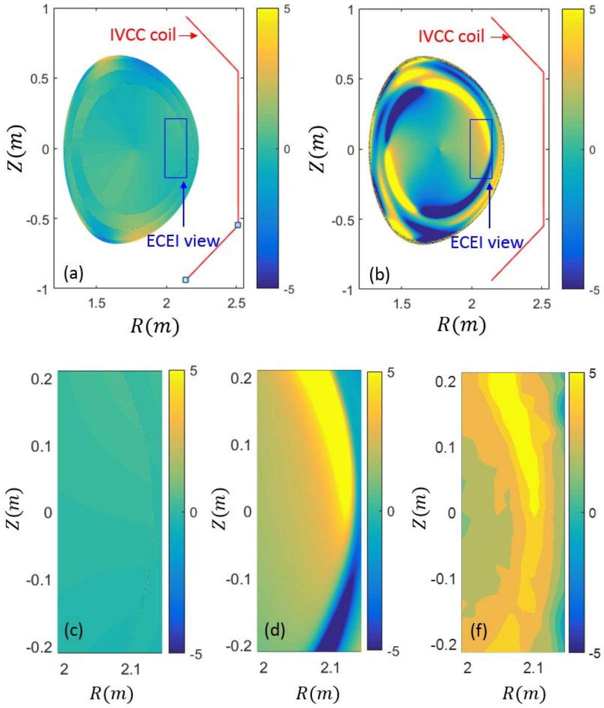

Figure 4.4 (color). Comparison of the computed radial plasma displacement (mm) of #19118 in KSTAR (a), (c) without 3D resistive plasma response and (b), (d) with 3D resistive plasma response using MARS-K, and (e) estimated 2D displacement (mm/kA) by $\xi_n = -\delta T_e / |\nabla T_e|$ [5] using ECE and electron cyclotron emission imaging data ($\delta T_e = \delta T_{e,t1} - \delta T_{e,t2}$) in #19118.

plasma response in the MARS-K simulation for the comparison. The comparison of the computed two different plasma response models is shown with the measured internal response structure in Fig. 4.4. One can see that the calculated displacement without resistive response is significantly smaller than the displacement with the resistive response. This clearly shows that the plasma displacement can be strongly amplified due to resistive field penetration by the resonant 3D field in KSTAR, which emphasizes the role of 3D resistive response. In particular, the 3D resistive plasma response strongly amplifies the displacement around the $q = 2$ surface. This localized structure can be confirmed by electron cyclotron emission imaging (ECEI) measurements around the $q = 2$ surface as shown in Fig. 4.4 (e). Note that the relation $\xi_n = -\delta T_e / |\nabla T_e|$ is assumed for estimating 2D displacement structure, where absolute value of T_e is given by the ECE measurement. The relation is applicable in the limit that $\vec{B} \cdot \nabla T_e = 0$ as illustrated in the Ref. Ferraro2013. For isolating the change of the T_e fluctuation level by the $n = 1$ field in ECEI, measurements at two different times before ($t_1 = 2.31 - 2.39s$) and after ($t_2 = 2.48 - 2.59s$) the $n = 1$ field application are subtracted in #19118. Although some artifacts from the system noise exist near $R \sim 2.13$ m, $Z \sim \pm 0.15$ m, the localized displacement structure and its magnitude observed by ECEI shows much better agreement with simulation result with 3D resistive response than without 3D resistive response. Note that a magnetic surface overlap would not occur in this case, even with the peaked displacement of $20mm$, as inferred from the $|d\xi_r/dr| < 1$, thus the linear calculation could be valid.

4.3.2 Estimating NTV torque

A calculation of NTV torque can be done by estimating non-ambipolar transport rate. In MARS-K, this is done by taking the imaginary part of the kinetic

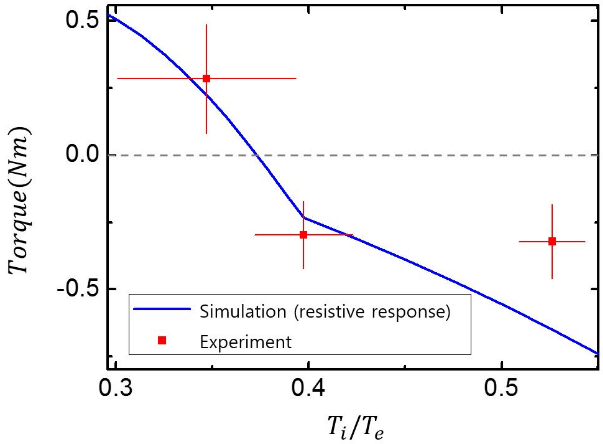

Figure 4.5 (color) Comparison of measured (black, square) and calculated NTV torque with (black, solid) and without (blue, dashed) resistive response in MARS-K simulations.

potential energy δW_k [75]. This has been benchmarked by different code using iPEC-PENT, MARS-K, and MARKS-Q code [19]. Using the MARS-K code, we also calculated NTV torque with/without including resistivity.

A calculation of electron NTV torque is also done by the MARS-K code, based on the equivalence between kinetic energy and NTV [19, 75]. However, those equivalence and calculations are difficult to apply for ions as the bouncing orbit is not well closed for ions, with $\nu_{*i} >> 1$. Instead, NTV formula derived at high collisionality regime which can be written as

$$\left\langle \hat{e}_t \cdot \vec{\nabla} \cdot \overleftrightarrow{\Pi} \right\rangle_p = \sum_{n,m\neq 0} \left(n^2 \left(\delta_L B_{nm}^2 \right) \frac{1}{\frac{2\sqrt{\pi}}{3\mu_{ps1}} \frac{\nu_i}{\frac{V_{Ti}}{R_0 q}} + |m - nq|} \right) \frac{\sqrt{\pi} p_i}{V_{Ti}} \left(\omega_\phi - \omega_{NC,i} \right), \tag{4.15}$$

which is similar to Eq. (4.15) in Ref. [Zhu2006]. As the variation of mangetic field strength, $\delta_L B_{nm}$, is given by the MARS-K result, the resistive plasma response can be included in this ion NTV calculation.

The calculated NTV torque also shows better agreement with expeirment by including resistive plasma response. The calculated NTV torque without the resistive response is around $10^{-3} Nm$ for #19115, which is much smaller than the experimental torque shown in Fig. 4.5. The experimental torque is estimated from the time evolution of the angular momentum density, $\partial L/\partial t$. The NBI torque calculated by NUBEAM [46] is around 0.55 Nm, supporting that a torque around $10^{-3} Nm$ would be insufficient to accelerate the plasma rotation. On the other hand, calculated NTV torque with resistive field penetration shown in Fig. 4.5 show better agreement with experiment. The electron NTV torque is mainly dominated by the precession resonance of thermal electrons in the presence of the resistive plasma response. The importance of resistive field penetraion on the estimated NTV torque can be understood by the differences in the displacement profiles in Fig. 4.4, as $\delta_L \vec{B} = \delta_E \vec{B} + \vec{\xi} \cdot \vec{B_0}$. The calculated NTV torque in Fig. 4.5 also show that magnetic accleration by electrons is possible with $T_e \gg T_i$. As the ion temperature (T_i/T_e) increases due to increased NBI power, ion NTV becomes comparable to electron NTV and flips sign from co-I_p to counter-I_p direction. This sign flip of the torque is consistent with the experimental observation. A more precise calculation with first-principle code [76] can further clarify the result in the future, which may yield additional negative NTV torque.

Chapter 5

Conclusions and future work

Stability and transport properties of tokamak plasmas have been studied using 3D-field-driven rotation. Mode locking threshold, turbulent momentum pinch, and NTV have been examined utilizing the 3D field in KSTAR.

Chapter 2 described the threshold of locked mode by the 3D magnetic field in ohmic discharges. This mode locking threshold has shown relatively weak density dependence in KSTAR. We found that the density dependence in KSTAR can be related to the change of the confinement regime. The density dependence of mode locking threshold in LOC regime has relatively stronger dependence than SOC regime in KSTAR. This transition of density dependence can be explained by extending the theoretical scaling from LOC to SOC regimes, and relatively weak density dependence in the locked mode thresholds is obtained in SOC. An electron NTV, which has been ignored in previous theory will be further included in the KSTAR scaling, as the electron NTV is a strong candidate to explain co-current observed in KSTAR with $T_e > T_i$.

Chapter 3 showed a presence of turbulent momentum pinch term in KSTAR. The quiescent braking by non-resonant 3D fields allows quantification of the effect of T_i perturbation in perturbative momentum transport analysis. We found that the presence of T_i perturbation can lead to overestimation of momentum transport coefficient in KSTAR, as shown by both the linearized equation and time-dependent transport simulations. The improved analysis method to extract momentum transport coefficients has been proposed, which can extract momentum transport coefficients even with the T_i perturbation. As the time-constant transport coefficients assumption might be inappropriate for the perturbative experiment using NBI, the proposed method may improve the previous results in KSTAR and other devices.

Chapter 4 described the acceleration of plasma rotation by the 3D magnetic field. The acceleration of toroidal rotation due to a 3D magnetic field is found in KSTAR L-mode discharge. On the other hand, in the faster-rotating plasmas in the $co - I_P$ direction with slightly higher NBI power, one can see the braking of rotation by the 3D magnetic field. This offset rotation behavior is found to be relevant to the electron neoclassical offset frequency and T_e/T_i in this study. The acceleration is related to the higher temperature of electrons than ions ($T_e \gg T_i$) in KSTAR. The numerical simulation further offers the quantitative explanations on the internal $n = 1$ structure detected by electron-cyclotron-emission imaging and the co-current plasma spinning observed in the experiments. This implies that strong magnetic acceleration can be originated from the amplified $\delta\vec{B}$ due to resistive field penetration which is self-consistently regulated by accompanying non-ambipolar electron currents.

These initial results provide an deeper understanding of plasma stability and transport driven by the 3D field. However, the analysis is done at specific plasma conditions, where the plasma operating condition can change the applicable plasma model. The investigation of its feasibility will be further investigated in future experiments at various operating conditions.

Bibliography

[1] Eurofusion organization. "Tokamak Principle" : https://www.euro-fusion.org/2011/09/tokamak-principle-2/?view=gallery-11.

[2] Z. Lin, T. S. Hahm, W. W. Lee, W. M. Tang, and R. B. White. Turbulent transport reduction by zonal flows: massively parallel simulations. *Science (New York, N.Y.)*, 281(5384):1835–7, sep 1998.

[3] Doohyun Kim, Hyunsun Han, Ki Min Kim, Jong Kyu Park, Young Mu Jeon, Yong Su Na, and Sang Hee Hong. Numerical simulation on edge localized mode control capability of resonant magnetic perturbation in the KSTAR tokamak. *Plasma Physics and Controlled Fusion*, 52(9), 2010.

[4] Y. M. Jeon, J. K. Park, S. W. Yoon, W. H. Ko, S. G. Lee, K. D. Lee, G. S. Yun, Y. U. Nam, W. C. Kim, Jong Gu Kwak, K. S. Lee, H. K. Kim, and H. L. Yang. Suppression of edge localized modes in high-confinement KSTAR plasmas by nonaxisymmetric magnetic perturbations. *Physical Review Letters*, 109(3):1–5, 2012.

[5] N. M. Ferraro, T. E. Evans, L. L. Lao, R. A. Moyer, R. Nazikian, D. M. Orlov, M. W. Shafer, E. A. Unterberg, M. R. Wade, and A. Wingen. Role

of plasma response in displacements of the tokamak edge due to applied non-axisymmetric fields. *Nuclear Fusion*, 53(7), 2013.

[6] A. M. Garofalo, E. J. Strait, L. C. Johnson, R. J. La Haye, E. A. Lazarus, G. A. Navratil, M. Okabayashi, J. T. Scoville, T. S. Taylor, and A. D. Turnbull. Sustained Stabilization of the Resistive-Wall Mode by Plasma Rotation in the DIII-D Tokamak. *Physical Review Letters*, 89(23):235001, nov 2002.

[7] R. J. Buttery, R. J. La Haye, P. Gohil, G. L. Jackson, H. Reimerdes, and E. J. Strait. The influence of rotation on the βN threshold for the 21 neoclassical tearing mode in DIII-D. *Physics of Plasmas*, 15(5):056115, may 2008.

[8] H. Biglari, P. H. Diamond, and P. W. Terry. Influence of sheared poloidal rotation on edge turbulence. *Physics of Fluids B: Plasma Physics*, 2(1):1–4, jan 1990.

[9] T. S. Hahm and K. H. Burrell. Flow shear induced fluctuation suppression in finite aspect ratio shaped tokamak plasma. *Physics of Plasmas*, 2(5):1648–1651, may 1995.

[10] K. H. Burrell. Effects of E$\times$B velocity shear and magnetic shear on turbulence and transport in magnetic confinement devices. *Physics of Plasmas*, 4(5):1499–1518, may 1997.

[11] J. D. Callen, A. J. Cole, and C. C. Hegna. Toroidal rotation in tokamak plasmas. *Nuclear Fusion*, 49(8), 2009.

[12] K. C. Shaing. Magnetohydrodynamic-activity-induced toroidal momentum dissipation in collisionless regimes in tokamaks. *Physics of Plasmas*, 10(5):1443–1448, may 2003.

[13] K. C. Shaing and J. D. Callen. Neoclassical flows and transport in nonaxisymmetric toroidal plasmas. *Physics of Fluids*, 26(11):3315–3326, 1983.

[14] R. Fitzpatrick. Interaction of tearing modes with external structures in cylindrical geometry (plasma). *Nuclear Fusion*, 33(7):1049–1084, 1993.

[15] R. J. Buttery, M. De Benedetti, D. A. Gates, Yu Gribov, T. C. Hender, R. J. La Haye, P. Leahy, J. A. Leuer, A. W. Morris, A. Santagiustina, J. T. Scoville, and B. J.D. Tubbing. Error field mode studies on JET, COMPASS-D and DIII-D, and implications for ITER. *Nuclear Fusion*, 39(Special Issu):1827–1835, 1999.

[16] S. M. Wolfe, I. H. Hutchinson, R. S. Granetz, J. Rice, A. Hubbard, A. Lynn, P. Phillips, T. C. Hender, D. F. Howell, R. J. La Haye, and J. T. Scoville. Nonaxisymmetric field effects on Alcator C-Mod. *Physics of Plasmas*, 12(5):1–10, 2005.

[17] D. F. Howell, T. C. Hender, and G. Cunningham. Locked mode thresholds on the MAST spherical tokamak. *Nuclear Fusion*, 47(9):1336–1340, 2007.

[18] J. E. Menard, R. E. Bell, D. A. Gates, S. P. Gerhardt, J. K. Park, S. A. Sabbagh, J. W. Berkery, A. Egan, J. Kallman, S. M. Kaye, B. Leblanc, Y. Q. Liu, A. Sontag, D. Swanson, H. Yuh, and W. Zhu. Progress in understanding error-field physics in NSTX spherical torus plasmas. *Nuclear Fusion*, 50(4), 2010.

[19] Zhirui Wang, Jong Kyu Park, Yueqiang Liu, Nikolas Logan, Kimin Kim, and Jonathan E. Menard. Theory comparison and numerical benchmarking on neoclassical toroidal viscosity torque. *Physics of Plasmas*, 21(4), 2014.

[20] A. J. Cole, C. C. Hegna, and J. D. Callen. Effect of Neoclassical Toroidal Viscosity on Error-Field Penetration Thresholds in Tokamak Plasmas. *Phys. Rev. Lett.*, 99(6):65001, 2007.

[21] R. Fitzpatrick. Nonlinear error-field penetration in low density ohmically heated tokamak plasmas. *Plasma Physics and Controlled Fusion*, 54(9), 2012.

[22] Y. In, J. K. Park, J. M. Jeon, J. Kim, and M. Okabayashi. Extremely low intrinsic non-axisymmetric field in KSTAR and its implications. *Nuclear Fusion*, 55(4), 2015.

[23] Jong-kyu Park, Allen H. Boozer, and Alan H. Glasser. Computation of three-dimensional tokamak and spherical torus equilibria. *Physics of Plasmas*, 14(5):052110, may 2007.

[24] D.H. Na, Yong-Su Na, S.G. Lee, C. Angioni, S.M. Yang, H.-S. Kim, T.S. Hahm, W.H. Ko, H. Jhang, and W.J. Lee. Observation of the intrinsic rotation in KSTAR Ohmic L-mode plasmas. *Nuclear Fusion*, 56(3):036011, mar 2016.

[25] P.N. Yushmanov, T. Takizuka, K.S. Riedel, O.J.W.F. Kardaun, J.G. Cordey, S.M. Kaye, and D.E. Post. Scalings for tokamak energy confinement. *Nuclear Fusion*, 30(10):1999–2006, oct 1990.

[26] P.H. Diamond, C.J. McDevitt, Ö.D. Gürcan, T.S. Hahm, W. X. Wang, E.S. Yoon, I. Holod, Z. Lin, V. Naulin, and R. Singh. Physics of non-

diffusive turbulent transport of momentum and the origins of spontaneous rotation in tokamaks. *Nuclear Fusion*, 49(4):045002, apr 2009.

[27] T. S. Hahm, P. H. Diamond, O. D. Gurcan, and G. Rewoldt. Nonlinear gyrokinetic theory of toroidal momentum pinch. *Physics of Plasmas*, 14(7):072302, jul 2007.

[28] A. G. Peeters, C. Angioni, and D. Strintzi. Toroidal Momentum Pinch Velocity due to the Coriolis Drift Effect on Small Scale Instabilities in a Toroidal Plasma. *Physical Review Letters*, 98(26):265003, jun 2007.

[29] K Nagashima, Y Koide, and H Shirai. Experimental determination of non-diffusive toroidal momentum flux in JT-60U. *Nuclear Fusion*, 34(3):449–454, mar 1994.

[30] M Yoshida, Y Koide, H Takenaga, H Urano, N Oyama, K Kamiya, Y Sakamoto, Y Kamada, and the JT-60 Team. Effects of ripple loss of fast ions on toroidal rotation in JT-60U. *Plasma Physics and Controlled Fusion*, 48(11):1673–1681, nov 2006.

[31] K. Ida, Y. Miura, T. Matsuda, K. Itoh, S. Hidekuma, S.-I. Itoh, and S.-I. JFT-2M Group. Evidence for a Toroidal-Momentum-Transport Non-diffusive Term from the JFT-2M Tokamak. *Physical Review Letters*, 74(11):1990–1993, mar 1995.

[32] W. D. Lee, J. E. Rice, E. S. Marmar, M. J. Greenwald, I. H. Hutchinson, and J. A. Snipes. Observation of Anomalous Momentum Transport in Tokamak Plasmas with No Momentum Input. *Physical Review Letters*, 91(20):205003, nov 2003.

[33] T Tala, K Crombé, P C de Vries, J Ferreira, P Mantica, A G Peeters, Y Andrew, R Budny, G Corrigan, A Eriksson, X Garbet, C Giroud, M-D Hua, H Nordman, V Naulin, M F F Nave, V Parail, K Rantamäki, B D Scott, P Strand, G Tardini, A Thyagaraja, J Weiland, and K-D Zastrow. Toroidal and poloidal momentum transport studies in tokamaks. *Plasma Physics and Controlled Fusion*, 49(12B):B291–B302, dec 2007.

[34] T. Tala, K.-D. Zastrow, J. Ferreira, P. Mantica, V. Naulin, A. G. Peeters, G. Tardini, M. Brix, G. Corrigan, C. Giroud, and D. Strintzi. Evidence of Inward Toroidal Momentum Convection in the JET Tokamak. *Physical Review Letters*, 102(7):075001, feb 2009.

[35] W. M. Solomon, S. M. Kaye, R. E. Bell, B. P. LeBlanc, J. E. Menard, G. Rewoldt, W. Wang, F. M. Levinton, H. Yuh, and S. A. Sabbagh. Momentum-Transport Studies in High E $\times$ B Shear Plasmas in the National Spherical Torus Experiment. *Physical Review Letters*, 101(6):065004, aug 2008.

[36] W.M. Solomon, K.H. Burrell, A.M. Garofalo, A.J. Cole, R.V. Budny, J.S. DeGrassie, W.W. Heidbrink, G.L. Jackson, M.J. Lanctot, R. Nazikian, H. Reimerdes, E.J. Strait, and M.A. Van Zeeland. Advances in understanding the generation and evolution of the toroidal rotation profile on DIII-D. *Nuclear Fusion*, 49(8):085005, aug 2009.

[37] D.H. Na, Yong-Su Na, C. Angioni, S.M. Yang, J.M. Kwon, Hogun Jhang, Y. Camenen, S.G. Lee, Y.J. Shi, W.H. Ko, J.A. Lee, and T.S. Hahm. A comprehensive study on rotation reversal in KSTAR: experimental observations and modelling. *Nuclear Fusion*, 57(12):126008, dec 2017.

[38] W. Guttenfelder, A.R. Field, I. Lupelli, T. Tala, S.M. Kaye, Y. Ren, and W.M. Solomon. Perturbative momentum transport in MAST L-mode plasmas. *Nuclear Fusion*, 57(5):056022, may 2017.

[39] M. Yoshida, S. Kaye, J. Rice, W. Solomon, T. Tala, R.E. Bell, K.H. Burrell, J. Ferreira, Y. Kamada, D. McDonald, P. Mantica, Y. Podpaly, M.L. Reinke, Y. Sakamoto, and A. Salmi. Momentum transport studies from multi-machine comparisons. *Nuclear Fusion*, 52(12):123005, dec 2012.

[40] K. W. Gentle. Dependence of heat pulse propagation on transport mechanisms: Consequences of nonconstant transport coefficients. *Physics of Fluids*, 31(5):1105, 1988.

[41] Won-Ha Ko, Hyungho Lee, Dongcheol Seo, and Myeun Kwon. Charge exchange spectroscopy system calibration for ion temperature measurement in KSTAR. *Review of Scientific Instruments*, 81(10):10D740, oct 2010.

[42] P. Mantica, T. Tala, J. S. Ferreira, A. G. Peeters, A. Salmi, D. Strintzi, J. Weiland, M. Brix, C. Giroud, G. Corrigan, V. Naulin, G. Tardini, and K.-D. Zastrow. Perturbative studies of toroidal momentum transport using neutral beam injection modulation in the Joint European Torus: Experimental results, analysis methodology, and first principles modeling. *Physics of Plasmas*, 17(9):092505, sep 2010.

[43] W. Zhu, S. A. Sabbagh, R. E. Bell, J. M. Bialek, M. G. Bell, B. P. LeBlanc, S. M. Kaye, F. M. Levinton, J. E. Menard, K. C. Shaing, A. C. Sontag, and H. Yuh. Observation of Plasma Toroidal-Momentum Dissipation by Neoclassical Toroidal Viscosity. *Physical Review Letters*, 96(22):225002, jun 2006.

[44] Jong-kyu Park, Allen H. Boozer, Jonathan E. Menard, Andrea M. Garofalo, Michael J. Schaffer, Richard J. Hawryluk, Stanley M. Kaye, Stefan P. Gerhardt, and Steve A. Sabbagh. Importance of plasma response to nonaxisymmetric perturbations in tokamaks. *Physics of Plasmas*, 16(5):056115, may 2009.

[45] J.-K. Park, Y. M. Jeon, J. E. Menard, W. H. Ko, S. G. Lee, Y. S. Bae, M. Joung, K.-I. You, K.-D. Lee, N. Logan, K. Kim, J. S. Ko, S. W. Yoon, S. H. Hahn, J. H. Kim, W. C. Kim, Y.-K. Oh, and J.-G. Kwak. Rotational Resonance of Nonaxisymmetric Magnetic Braking in the KSTAR Tokamak. *Physical Review Letters*, 111(9):095002, aug 2013.

[46] Alexei Pankin, Douglas McCune, Robert Andre, Glenn Bateman, and Arnold Kritz. The tokamak Monte Carlo fast ion module NUBEAM in the national transport code collaboration library. *Computer Physics Communications*, 159(3):157–184, 2004.

[47] Nikolas C. Logan, Jong-Kyu Park, Kimin Kim, Zhirui Wang, and John W. Berkery. Neoclassical toroidal viscosity in perturbed equilibria with general tokamak geometry. *Physics of Plasmas*, 20(12):122507, dec 2013.

[48] G V Pereverzev and P N Yushmanov. {ASTRA} {A}utomated {S}ystem for {TR}ansport {A}nalysis in a {T}okamak. (5/98), 2002.

[49] I. Holod and Z. Lin. Gyrokinetic particle simulations of toroidal momentum transport. *Physics of Plasmas*, 15(9):092302, sep 2008.

[50] A. G. Peeters, Y. Camenen, F. J. Casson, W. A. Hornsby, A. P. Snodin, D. Strintzi, and G. Szepesi. The nonlinear gyro-kinetic flux tube code GKW. *Computer Physics Communications*, 180(12):2650–2672, 2009.

[51] H. Lütjens, A. Bondeson, and O. Sauter. The CHEASE code for toroidal MHD equilibria. *Computer Physics Communications*, 97(3):219–260, 1996.

[52] X Garbet, P Mantica, C Angioni, E Asp, Y Baranov, C Bourdelle, R Budny, F Crisanti, G Cordey, L Garzotti, N Kirneva, D Hogeweij, T Hoang, F Imbeaux, E Joffrin, X Litaudon, A Manini, D C McDonald, H Nordman, V Parail, A Peeters, F Ryter, C Sozzi, M Valovic, T Tala, A Thyagaraja, I Voitsekhovitch, J Weiland, H Weisen, A Zabolotsky, and the JET EFDA Contributors. Physics of transport in tokamaks. *Plasma Physics and Controlled Fusion*, 46(12B):B557–B574, dec 2004.

[53] N. Mattor and P. H. Diamond. Momentum and thermal transport in neutral-beam-heated tokamaks. *Physics of Fluids*, 31(5):1180, 1988.

[54] A. G. Peeters and C. Angioni. Linear gyrokinetic calculations of toroidal momentum transport in a tokamak due to the ion temperature gradient mode. *Physics of Plasmas*, 12(7):072515, jul 2005.

[55] A G Peeters, C Angioni, A Bottino, A Kallenbach, B Kurzan, C F Maggi, W Suttrop, and the ASDEX Upgrade Team. Toroidal momentum transport. *Plasma Physics and Controlled Fusion*, 48(12B):B413–B420, dec 2006.

[56] T. Tala, A. Salmi, C. Angioni, F.J. Casson, G. Corrigan, J. Ferreira, C. Giroud, P. Mantica, V. Naulin, A.G. Peeters, W.M. Solomon, D. Strintzi, M. Tsalas, T.W. Versloot, P.C. de Vries, and K.-D. Zastrow. Parametric dependences of momentum pinch and Prandtl number in JET. *Nuclear Fusion*, 51(12):123002, dec 2011.

[57] S. Ku, J. Abiteboul, P.H. Diamond, G. Dif-Pradalier, J.M. Kwon, Y. Sarazin, T.S. Hahm, X. Garbet, C.S. Chang, G. Latu, E.S. Yoon,

Ph. Ghendrih, S. Yi, A. Strugarek, W. Solomon, and V. Grandgirard. Physics of intrinsic rotation in flux-driven ITG turbulence. *Nuclear Fusion*, 52(6):063013, jun 2012.

[58] A. M. Garofalo, K. H. Burrell, J. C. Deboo, J. S. Degrassie, G. L. Jackson, M. Lanctot, H. Reimerdes, M. J. Schaffer, W. M. Solomon, and E. J. Strait. Observation of plasma rotation driven by static nonaxisymmetric magnetic fields in a tokamak. *Physical Review Letters*, 101(19):1–4, 2008.

[59] K. H. Finken, S. S. Abdullaev, M. F.M. De Bock, M. Von Hellermann, M. Jakubowski, R. Jaspers, H. R. Koslowski, A. Krämer-Flecken, M. Lehnen, Y. Liang, A. Nicolai, R. C. Wolf, O. Zimmermann, M. De-Baar, G. Bertschinger, W. Biel, S. Brezinsek, C. Busch, A. J.H. Donné, H. G. Esser, E. Farshi, H. Gerhauser, B. Giesen, D. Harting, J. A. Hoekzema, G. M.D. Hogeweij, P. W. Hüttemann, S. Jachmich, K. Jakubowska, D. Kalupin, F. Kelly, Y. Kikuchi, A. Kirschner, R. Koch, M. Korten, A. Kreter, J. Krom, U. Kruezi, A. Lazaros, A. Litnovsky, X. Loozen, N. J.Lopes Cardozo, A. Lyssoivan, O. Marchuk, G. Matsunaga, Ph Mertens, A. Messiaen, O. Neubauer, N. Noda, V. Philipps, A. Pospieszczyk, D. Reiser, D. Reiter, A. L. Rogister, M. Sakamoto, A. Savtchkov, U. Samm, O. Schmitz, R. P. Schorn, B. Schweer, F. C. Schüller, G. Sergienko, K. H. Spatschek, G. Telesca, M. Tokar, R. Uhlemann, B. Unterberg, G. Van Oost, T. Van Rompuy, G. Van Wassenhove, E. Westerhof, R. Weynants, S. Wiesen, and Y. H. Xu. Toroidal plasma rotation induced by the dynamic ergodic divertor in the TEXTOR tokamak. *Physical Review Letters*, 94(1):1–5, 2005.

[60] K. J. Zhao, Yuejiang Shi, H. Liu, P. H. Diamond, F. M. Li, J. Cheng, Z. P. Chen, L. Nie, Y. H. Ding, Y. F. Wu, Z. Y. Chen, B. Rao, Z. F. Cheng,

L. Gao, X. Q. Zhang, Z. J. Yang, N. C. Wang, L. Wang, W. Jin, J. Q. Xu, L. W. Yan, J. Q. Dong, and G. Zhuang. Co-current toroidal rotation-driven and turbulent stresses with resonant magnetic perturbations in the edge plasmas of the J-TEXT tokamak. *Nuclear Fusion*, 56(7), 2016.

[61] K. C. Shaing, K. Ida, and S. A. Sabbagh. Neoclassical plasma viscosity and transport processes in non-axisymmetric tori. *Nuclear Fusion*, 55(12):125001, 2015.

[62] Y. B. Kim, P. H. Diamond, and R. J. Groebner. Neoclassical poloidal and toroidal rotation in tokamaks. *Physics of Fluids B*, 3(8):2050–2060, 1991.

[63] J. D. Callen. Effects of 3D magnetic perturbations on toroidal plasmas. *Nuclear Fusion*, 51(9), 2011.

[64] S. A. Sabbagh, Y. S. Park, J Kim, W. H. Ko, S. H. Hahn, Y In, Y. K. Oh, K. C. Shaing, and Y Sun. Observation of the Generalized Neoclassical Toroidal Viscosity Offset Rotation Profile in KSTAR. In *APS Meeting Abstracts*, page NO4.007, 2017.

[65] T. C. Hender, R. Fitzpatrick, A. W. Morris, P. G. Carolan, R. D. Durst, T. Edlington, J. Ferreira, S. J. Fielding, P. S. Haynes, J. Hugill, I. J. Jenkins, R. J. La Haye, B. J. Parham, D. C. Robinson, T. N. Todd, M. Valovic, and G. Vayakis. Effect of resonant magnetic perturbations on COMPASS-C tokamak discharges. *Nuclear Fusion*, 32(12):2091–2117, 1992.

[66] Shinsuke Satake, Hideo Sugama, Ryutaro Kanno, and Jong Kyu Park. Calculation of neoclassical toroidal viscosity in tokamaks with broken toroidal symmetry. *Plasma Physics and Controlled Fusion*, 53(5), 2011.

[67] Kimin Kim, Jong Kyu Park, Gerrit J Kramer, and Allen H Boozer. f Monte Carlo calculation of neoclassical transport in perturbed tokamaks. *Physics of Plasmas*, 19(8), 2012.

[68] R. J. La Haye, A. W. Hyatt, and J. T. Scoville. Nonlinear instability to low m,n=1 error fields in DIII-D as a function of plasma fluid rotation and beta. *Nuclear Fusion*, 32(12):2119–2126, 1992.

[69] E Lazzaro, R J Buttery, T C Hender, P Zanca, R Fitzpatrick, M Bigi, T Bolzonella, R Coelho, M DeBenedetti, S Nowak, O Sauter, and M Stamp. Error field locked modes thresholds in rotating plasmas, anomalous braking and spin-up. *Physics of Plasmas*, 9(9):3906, 2002.

[70] W. M. Solomon, K. H. Burrell, J. S. Degrassie, R. Budny, R. J. Groebner, J. E. Kinsey, G. J. Kramer, T. C. Luce, M. A. Makowski, D. Mikkelsen, R. Nazikian, C. C. Petty, P. A. Politzer, S. D. Scott, M. A. Van Zeeland, and M. C. Zarnstorff. Momentum confinement at low torque. *Plasma Physics and Controlled Fusion*, 49(12 B), 2007.

[71] J.-K. Park. Ideal Perturbed Equilibria in Tokamaks. *Princeton University*, page 304, 2009.

[72] Jong Kyu Park and Nikolas C. Logan. Self-consistent perturbed equilibrium with neoclassical toroidal torque in tokamaks. *Physics of Plasmas*, 24(3), 2017.

[73] Yueqiang Liu, M S Chu, I T Chapman, and T C Hender. Toroidal self-consistent modeling of drift kinetic effects on the resistive wall mode. *Physics of Plasmas*, 15(11), 2008.

[74] Z. R. Wang, M. J. Lanctot, Y. Q. Liu, J. K. Park, and J. E. Menard. Three-dimensional drift kinetic response of high-β plasmas in the DIII-D tokamak. *Physical Review Letters*, 114(14):1–5, 2015.

[75] Jong Kyu Park. Kinetic energy principle and neoclassical toroidal torque in tokamaks. *Physics of Plasmas*, 18(11), 2011.

[76] Kimin Kim, Jong Kyu Park, and Allen H. Boozer. Numerical verification of bounce-harmonic resonances in neoclassical toroidal viscosity for tokamaks. *Physical Review Letters*, 110(18):1–5, 2013.

초록

토카막 플라즈마에서는 작은 크기의 3차원 자기장도 플라즈마 안정성이나 가둠 성능성에 크게 영향을 줄 수 있다. 이러한 영향의 근본적인 메커니즘은 주로 토로이덜 방향의 대칭이 깨질 때 나타나는 전자기적 토크와 관련이 있으며 이는 플라즈마의 가둠 특성과 안정성에 영향을 미치는 토로이덜 방향 회전을 변화시키며 나타나게 된다. 이 논문은 KSTAR 토카막 플라즈마에 3차원 자기자기 인가했을 때 나타나는 다양한 토크와 플라즈마 회전 변화에 대해 연구하였으며 그 중 몇 가지 중요한 결과에 대해 다룬다. 이는 플라즈마와 공명하는 토크에 의해 발생하는 급격한 플라즈마 회전 감소 및 풀라즈마 붕괴 현상 (락모드) 과 비 공명하는 토크에 (NTV) 의해 새로운 운동량 균형에 도달하는 느린 플라즈마 회전 변화에 관한 내용이다.

락모드는 공명하는 3차원 자기장에 의한 토크가 균형을 이루던 플라즈마의 점성에 의한 토크보다 충분히 커질 때 공진 표면에서 자기 재결합을 일으킬 때에 관측된다. 다수의 토카막 장차들의 실험 결과들은 락모드발생의 임계점이 플라즈마 밀도에 선형적으로 비례한다고 보이는 반면 KSTAR 장치의 밀도 의존성은 그보다 훨씬 약한 것으로 관측되었다. 하지만 특정 수송특징을 가진 영역에 대해서는 KSTAR 에서도 밀도에 대한 선형 의존성이 다시 회복되었다. 한편으로는 락모드의 발생에 영향을 줄 수 있는 운동량 수송이 수송특징의 변화에 따라 바뀌었기 때문에 이러한 결과를 얻었다고 생각해 볼 수 있다. 이러한 토카막 플라즈마 내의 운동량 수송은 미세난류에 의해 결정된다고 알려져 있다. 또한 이러한 운동량 수송의 비확산 수송 특성은 토크 변조 실험을 통해 정량적으로 추론해 볼 수 있음이 잘 알려져 있다. 그러나 이러한 과도상태 분석 방법은 입자나 열 수송 체널에도 영향을 줄 수 있기 때문에 기존에 수행된 방법론 보다 더 주의를 기울여 수행할 필요가 있다. 본 연구는 토크가 3차원 자기장이 아니라 중성 입자 빔에 의해 변조되었을 때에 나타나는 운동량 핀치 계수의 불일치가 중성입자 빔이 만드는 이온 온도 변화 때문이라고 설명한다. 본 논문의 또다른 중요한 결과는 3차원 자기장에

의해 반경방향으로 이동하는 전자 때문에 발생하는 플라즈마 회전의 전체적인 증가 현상을 확인한 사실이다. 이러한 관측은 상호 보완적인 MHD 전산모사를 통해 검증 되었으며, 실험에서 관측된 플라즈마 전류방향으로의 회전 증가를 정량적으로 설명할 수 있음이 확인되었다.

이러한 KSTAR 에서의 연구결과는 3차원 자기장의 효과를 이하는데 도움을 주었다. 3차원 자기장에 의한 플라즈마 반응은 이상 자기유체로도 설명 가능하나 특정 상황에서는 플라즈마의 저항또한 같이 고려해야할 필요가 있었다. 적용 가능한 플라즈마 모델과 이의 타당성은 이후 다양한 조건에서의 실험을 통해 확인 되어질 예정이다

주요어: 토카막, 플라즈마 회전, 3D 자기장, KSTAR, NTV, 모드락킹, 운동량 수송
학번: 2013-21021